Steurer Elias, BSc

Design and Implementation of a Low Power Time-of-Flight Sensing Procedure

Master's Thesis

to achieve the university degree of

Diplom-Ingenieur

Master's degree programme: Information & Computer Engineering

submitted to

Graz University of Technology

Supervisor

Ass.Prof. Dipl.-Ing. Dr.techn. Steger Christian

Institute for Technical Informatics

Advisor

Ass.Prof. Dipl.-Ing. Dr.techn. Steger Christian
Dipl.-Ing. Dr.techn. Markus Dielacher (Infineon Technologies Austria AG)

Graz, September 2019

Kurzfassung

Der Einsatz von 3D Bildsensoren in mobilen Geräten hat in letzter Zeit vermehrt an Bedeutung gewonnen. Begünstigt wurde diese Entwicklung durch den immer kleiner werdenden Formfaktor. Die Anwendungen reichen von Gesichtserkennung und Autofokus bis hin zu Augmented Reality. Structured light und Time-of-Flight (ToF) sind die hierbei die wichtigsten Technologien. In dieser Arbeit liegt der Schwerpunkt auf der indirekten ToF Messung. Ein solches System besteht typischerweise aus einer modulierten Beleuchtungseinheit und einem Bildsensor hinter einer Linse, mit Hilfe dessen die Phasenverschiebung, verursacht durch die Laufzeit ermittelt werden kann. Basierend auf dieser Information wird ein Tiefenbild erzeugt.

Die Akkulaufzeit ist ein wichtiger Aspekt im mobilen Einsatzbereich. Mit der stetig steigenden Anzahl von Sensoren in Smartphones steigt auch der Stromverbrauch des Gesamtsystems. Das Ziel dieser Arbeit ist die Entwicklung einer stromsparenden ToF Messarchitektur, die in der Lage ist, den Energiebedarf effektiv zu reduzieren und gleichzeitig eine Tiefenmessung im Nahbereich zu ermöglichen. Darüber hinaus sollte ein Vergleich mit bestehenden Proximity Sensoren gemacht werden.

Durch die Halbierung der Anzahl von Rohbildern von vier auf zwei kann eine erhebliche Energieeinsparung erreicht werden. Hierdurch kommen jedoch zusätzliche systematische Fehler zum Tragen. Um deren Einfluss auf die Tiefenberechnung zu ermitteln, wird ein bestehendes ToF Simulationsmodell erweitert und Messungen werden durchgeführt. Basierend auf dieser Analyse werden Fehlerkorrekturmechanismen entwickelt. Der vorgeschlagene Ansatz weist eine ähnliche Genauigkeit im Vergleich zum 4-Phasen Algorithmus auf. Daher bildet er die Grundlage der vorgeschlagenen Messarchitektur. Weitere Verbesserungen hinsichtlich des Energieverbrauchs werden durch eine drastische Reduzierung der Idle Zeit bei niedriger Bildwiederholungsrate erreicht. Dies wird durch wiederholtes Neustarten des Sensors und Laden der Konfiguration aus einem externen Flash-Speicher realisiert.

Die Ergebnisse zeigen, dass die Messroutine in der Lage ist genaue Tiefenbilder zu generieren und hierbei gleichzeitig eine verbesserten Energiebilanz aufzuweisen. Das theoretisch ermittelte Leistungsprofil der entwickelten Lösung ist vergleichbar mit jener von bestehenden Proximity Sensoren.

Abstract

3D image sensors are becoming more popular in recent times. Due to the decreasing form-factor they are included in mobile devices supplementing existing 2D image sensors. Applications vary from secure face-unlock and auto-focus to augmented reality. Structured light and Time-of-Flight (ToF) are the main technologies involved. Throughout this thesis the emphasis will be on the indirect ToF sensing approach towards 3D image creation. Such a system typically consists of a modulated illumination unit and an image sensor behind a lens which indirectly measures the phase-shift caused by the travelling time of the emitted light. Based on this information, a depth image can be generated.

Battery lifetime is an important aspect when operating in mobile environments. As the number of sensors in smartphones steadily increase so does their contribution to the overall power consumption. The goal of this thesis is the development of a low-power ToF measurement architecture capable of effectively reducing the energy footprint while still providing depth sensing functionality in close range. Furthermore a comparison with existing proximity sensor solutions should be made.

When reducing the number of raw frames from two to four, a substantial energy reduction can be achieved. However, as a result, systematic errors are introduced. In order to asses their impact on the depth calculation, an existing ToF simulation model is extended and real-world measurements are conducted. Based on the foregoing analysis, error correction mechanisms are developed. After applying them, the proposed approach shows similar accuracy when compared to the standard 4-phase processing. Therefore it forms the basis of the low-power measurement architecture. Further improvements in the power profile are made by drastically reducing the idle time during low Frames Per Second (FPS) operation. This is established by repeatably restarting the sensor core and loading its configuration from an external flash memory.

Results show that the proposed measurement architecture is capable of providing accurate depth-images while operating with an improved energy footprint. The theoretical power profile of the developed solution is comparable with existing proximity sensor solutions.

Affidavit

I declare that I have authored this thesis independently, that I have not used other than the declared sources/resources, and that I have explicitly indicated all material which has been quoted either literally or by content from the sources used. The text document uploaded to TUGRAZonline is identical to the present master‘s thesis.

Date	Signature

Acknowledgements

This thesis was composed at the TU Graz in 2019. I want to thank the Institute of Technical Informatics, especially my advisor Ass.Prof. Dipl.-Ing. Dr. Christian Steger for his support.

Furthermore I want to give thanks to the Automotive Sense & Control department at Infineon, in particular Dr. Markus Dielacher for his thoughtful explanations and his guidance throughout the thesis. Additionally I am grateful for the help of the Application Engineering department for providing me sensor hardware and configurations.

Finally I want to seize the chance to give special thanks to my family and friends. Without their continuous support during my time on earth all this wouldn't have been possible. You've enriched my life in so many ways, thank you!

Graz, September 2019 Elias Steurer

Contents

List of Figures

List of Tables

Chapter 1

Introduction

3D imaging is an ever evolving topic in research and industry. There exist several ways of imaging techniques. They can be broadly categorized in Triangulation, Interferometry and Time-of-Flight (ToF) [BR16].

- Triangulation is used as so-called stereo-vision system which is inspired by the human depth-perception. It is a measurement approach where the target point is a vertex of a triangle and the other remaining points are known. The resulting angles of the known edges or the length of the base is measured. Subsequently the distance to the target can be calculated [Lan06].
- ToF exploits the time-delay or phase-shift of emitted light waves. This technique is further explained in the following Section 2.1.
- Interferometry is based on superposition of electromagnetic waves with the same frequency. The resulting intensity pattern is determined by the phase-difference between them. In-phase waves undergo constructive and out-of-phase waves destructive interference [OSY+13].

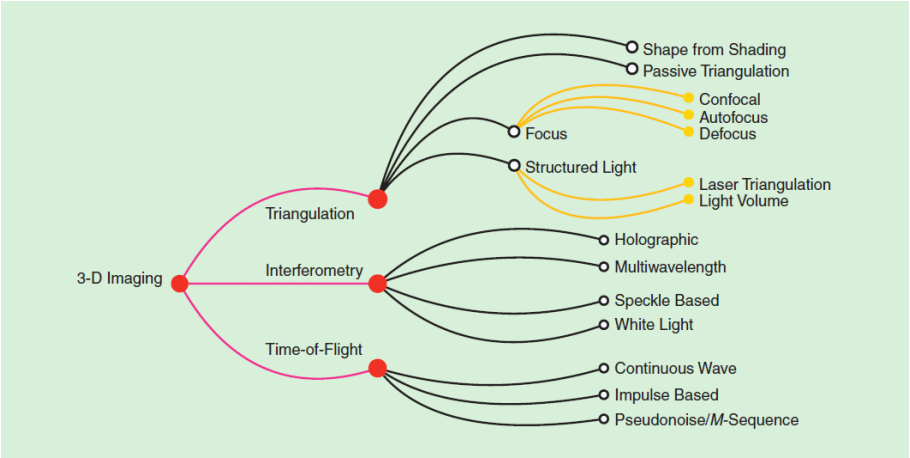

Figure 1.1: Classification of major 3-D imaging techniques [BR16].

The focus within this thesis is the ToF sensing approach towards 3D imaging working with CW modulated light in the infrared spectrum. By gathering several raw frames, a depth

and amplitude image can be subsequently generated. The scene is actively illuminated with IR light emitted by a light source which is incorporated in the imaging system. Therefore it is possible to operate even within complete darkness. An optical filter is placed in front of the sensor to mitigate wavelengths which are not of interest.

1.1 Motivation

In recent times ToF imaging systems were successfully miniaturized in order to integrate them in mobile devices. Due to limited battery capacity of such systems it is beneficial to reduce the power consumption of the involved components and/or integrate low-power operation modes. This thesis investigates the possibility to reduce the overall power consumption of an existing Infineon ToF sensor. Furthermore it has to be analyzed if it is possible to take over the functionality of a proximity sensor in a mobile phone utilizing a ToF imaging platform. Therefore the focus lies within techniques to reduce the overall power consumption while still providing depth sensing functionality. To achieve this a novel low-power processing architecture is presented after foregoing investigations regarding the involved error sources.

1.2 Objectives

In order to reduce the overall power consumption of the sensor system an existing simulation model should be extended to quantify error impacts on the measurement when operating with a reduced number of raw frames. Furthermore extensive analysis of deviations which cannot be simulated sufficiently should be made by evaluating real-world measurements. Based on the foregoing investigations a low-power measurement architecture integrating correction mechanisms is proposed. Conclusively this approach is analyzed regarding performance and limitations. The thesis covers the following tasks:

- Research the state of the art in the field of 3D ToF imaging and existing proximity sensor solutions incorporating their respective power profiles
- Investigation of the image sensor's power consumption in different use-cases and measurement states
- Analysis of the impact of systematic errors on the 2-phase depth calculation by means of simulation and real-world measurements
- Design and implementation of a low-power proximity sensing architecture
- Perform measurements in order to evaluate the proposed solution in comparison to the standard 4-phase measurement pipeline
- Evaluate the power profile of the proposed architecture and compare them with established proximity sensor solutions

1.3 Outline

The content of the thesis follows a structure described in this section. At the beginning the measurement principle of a typical 3D ToF imaging system is explained. The equations used for depth- and amplitude calculation are outlined and range extension is discussed. Subsequently the Photonic Mixing Device (PMD) is explained by investigating the internal mechanisms used to gather the correlation function between illumination- and modulation-signals. Each operation state of this device is mentioned due to its central connection to the overall power profile. This is followed by the theoretical description of the involved deviations which is done by categorizing them in systematic errors and noise sources. The state of the art in the field of the thesis marks the conclusion of the related work section.

After a brief explanation of the conventional processing pipeline and the power profile of the ToF imaging system, an extensive description of the impact of systematic errors is given. Furthermore the extensions of the simulation model and verification procedure for capturing real-world measurements are outlined. Based on the foregoing investigations a proximity sensing architecture is deducted and explained. Implementation details of the proposed solution and verification steps are given in the chapter 4. The accuracy of the error-corrected 2-phase measurement in comparison with the established 4-phase depth algorithm and the power profile of the low-power architecture are mentioned in chapter 5. Finally the conclusion and future work summarize the thesis and give suggestions for improvements.

Chapter 2

Related Work

This chapter describes the fundamentals of 3D-imaging based on Time-of-Flight (ToF) measurement. The various techniques are discussed briefly. However, the focus lies in the indirect ToF measurement and its physical working principle. Furthermore existing proximity sensors are analyzed in order to describe the state of the art in the field of the thesis.

2.1 Time-of-Flight

The principle of ToF in general is based on evaluating reflected light which is sent out by the illumination unit of an imaging system. As a consequence depth and amplitude information of the illuminated scene can be gathered. Typically, the wavelength of emitted light is chosen to be in the infrared spectrum. Care is taken to concentrate the sensitivity on this specific wavelength. 3D-imaging is enabled by combining several photo-sensitive units(pixels) together to form an image-sensor. These imaging systems can be further classified in two categories.

- Direct ToF systems evaluate the time-delay between emitted and received light pulses. This requires high accuracy on the receiver-side in order to detect the resulting small time-shifts within sufficient resolution [Alb07].
- Indirect ToF measurements on the other hand are conducted in Continuous-Wave (CW) mode. Modulated light is emitted continuously and the travelling time can be determined by evaluating the resulting phase-difference. As a consequence this measurement approach is called indirect. The focus within this thesis is the indirect ToF measurement. Therefore this approach is further examined in the following chapters.

2.2 Typical indirect ToF imaging setup

The following description applies to indirect ToF imaging systems working according to the PMD principle. A Vertical-cavity surface-emitting Laser (VCSEL) is utilized as a light-source to illuminate the scene. It is modulated by a continuous electrical signal and converts it into a corresponding optical emission.The phase-shift caused by the travelling

delay is evaluated based on information delivered by the pixels. This can be used to calculate a depth-image of the scene. Furthermore an Amplitude-Image can be constructed out of the same raw-data. Evaluation of this data is typically done by an Application-Processor connected to a dedicated high-speed MIPI Camera Serial Interface (CSI). Figure 2.1 gives an overview of a typical ToF imaging system.

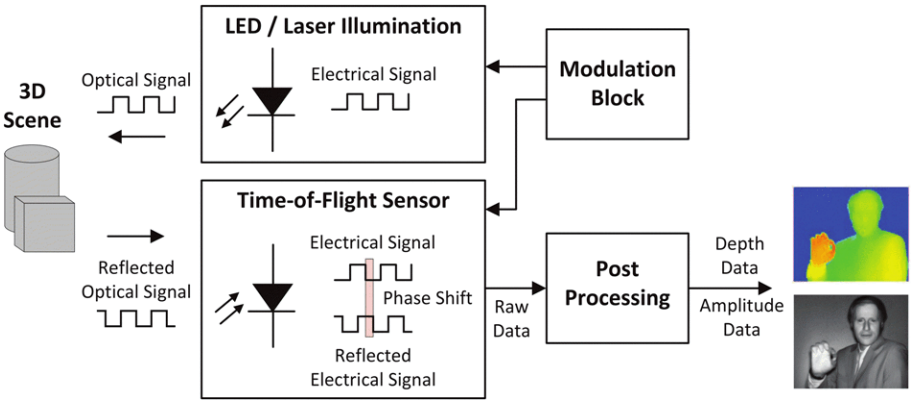

Figure 2.1: Typical indirect ToF 3-D imaging system [STHD17].

It is visible that the pixels are actively modulated during measurement. This happens in conjunction with actuating the illumination unit accordingly. The electrical signals used for modulation of the pixels and controlling of the light-source differ in real-world scenarios depending on the measurement.

2.2.1 Measurement Principle

Each pixel on the image sensor acts as a correlator. Therefore they perform an analog cross-correlation between the applied electrical modulation signal s and the received optical signal r. The respective voltage signals are digitized by several Analog Digital Converter (ADC)s. This mechanism is further explained in Section 2.2.2. The cross-correlation shown below in Equation 2.1 evaluates the similarity and implicitly the phase-lag between the two real signals r and s. τ is the additional phase-shift applied to the illumination signal. Typically 0°, 90°, 180° and 270° are used. For each of these phase-shifts a new phase-frame is sampled. This has to be done for every pixel of the image sensor [LSKK10].

$$c(t) = r \otimes s = \int_{-T/2}^{T/2} r(t) \cdot s(t+\tau) dt \tag{2.1}$$

If sinusoidal signals are used for modulation and illumination, the resulting cross-correlation function itself is sinusoidal. The maxima of this function indicate the points in time in which both signals do have the highest similarity. Subsequently the minima show the highest dissimilarity. As the cross-correlation directly relates to a certain phase-lag it can be used to determine the phase-shift between the emitted and received signal. In

figure 2.2 it is visible though that every shown correlation function does have the same values twice during one period. This yields two possible solutions. In order to resolve this unambiguity additional information is necessary. By using another 90° phase-shifted illumination-signal and subsequently calculating its cross-correlation in respect to the received signal this can be achieved. This establishes a complex phasor which provides unambiguous phase calculation within the interval $[0, 2\pi]$.

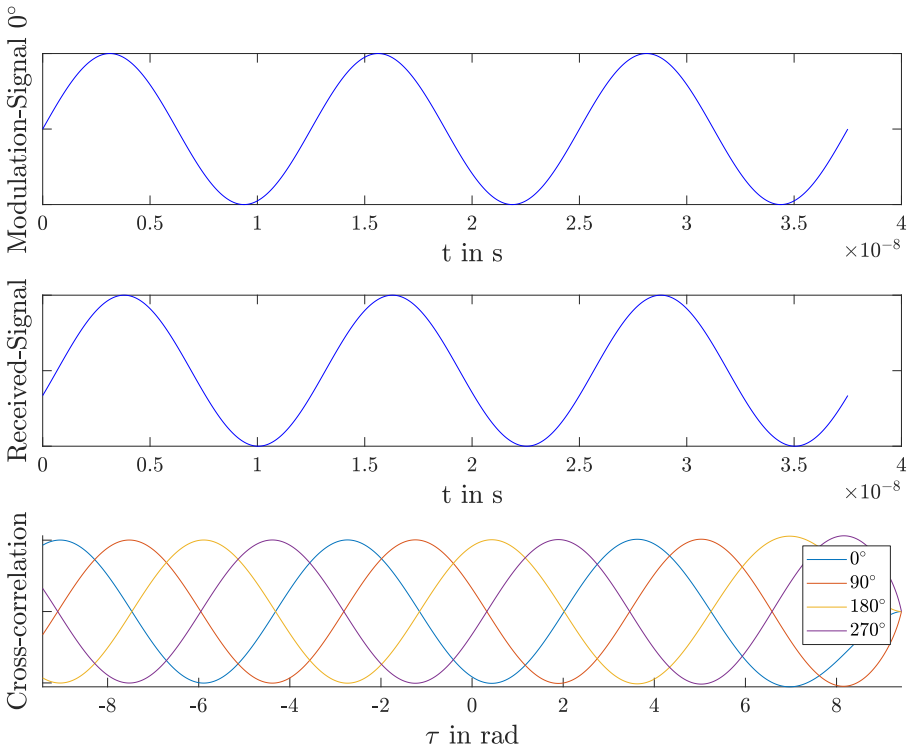

Figure 2.2: 4-phase sinusoidal cross-correlation functions.

2.2.1.1 Amplitude and Phase-Information

The respective values of the two cross-correlation functions can directly be used to calculate the phase-shift φ using the arctan function. In practice these values are obtained by digitizing the analog sensor output-voltage u_{pmd}.

$$\varphi_{ToF,2-phase} = \arctan \frac{u_{pmd,90°}}{u_{pmd,0°}} \tag{2.2}$$

Due to systematic errors introduced by the measurement using only two phases the above described procedure can lead to significant deviation compared to the actual phase-value. These errors will be addressed and explained later in section 2.3. By using a 4-phase algorithm a cancellation of some error-sources can be achieved. Therefore four sequential measurements using $n \cdot \Delta 90^\circ$ are conducted. This represents the so called $four - bucket$ algorithm shown in Equation 2.3 which is most commonly used for depth calculation. By using the information gathered it is additionally possible to calculate the amplitude and intensity image of the scene. Utilizing the above described 4-phase readout-voltages this leads to Equation 2.4 and 2.5 shown below [Lan06] .

$$\varphi_{ToF,4-phase} = \arctan \frac{u_{pmd,90^\circ} - u_{pmd,270^\circ}}{u_{pmd,0^\circ} - u_{pmd,180^\circ}} \tag{2.3}$$

$$A_{ToF,4-phase} = \frac{\sqrt{(u_{pmd,90^\circ} - u_{pmd,270^\circ})^2 + (u_{pmd,0^\circ} - u_{pmd,180^\circ})^2}}{2} \tag{2.4}$$

$$I_{ToF} = \frac{u_{pmd,0^\circ} + u_{pmd,90^\circ} - u_{pmd,180^\circ} - u_{pmd,270^\circ}}{4} \tag{2.5}$$

2.2.1.2 Relation between φ and the actual distance

In the previous descriptions operating at a single modulation frequency was assumed. As a consequence the calculation for the distance d follows equation 2.6 below. f_M is the modulation frequency, φ denoted the calculated phase-shift and c is the speed of light [JCPD10].

$$d = \frac{c}{2 \cdot f_M} \frac{\varphi}{2\pi} \tag{2.6}$$

The phase-shift φ is only uniquely defined within the interval $[0, 2\pi]$. Therefore if the phase-delay of the reflected light exceeds 2π the measurement is not unambiguous anymore. Points at larger distances may then appear close with respect to the ToF system. Consequently the maximum operating range using one modulation frequency is limited according to Equation 2.7.

$$d_u = \frac{c}{2 \cdot f_M} \tag{2.7}$$

Depth precision directly relates to the modulation frequency. If f_M is increased so does the resulting depth-resolution. On the other hand when looking at Equation 2.7 it can be seen that a higher modulation frequency also decreases the unambiguity range. To overcome this issue typically another 4-phase measurement using a different modulation

frequency is used. The information collected from both measurements are then combined into a single depth-image. Figure 2.3 shows a measurement utilizing two modulation frequencies f_1 and f_2. Those frequencies directly correspond to an unambiguity range of $1.875m$ and $2.5m$ respectively.

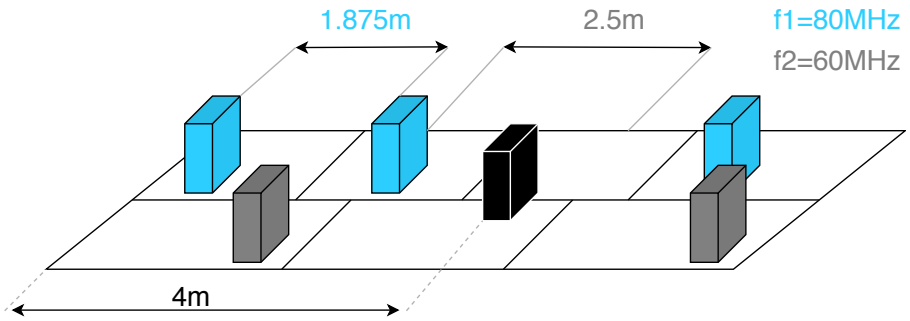

Figure 2.3: Range-Extension using two distinct modulation frequencies f_1 and f_2. The unambiguity range is shown for both frequencies. Obtained with changes from [PJD+09, JCPD10].

The real distance of the object in the scene shown above in figure 2.3 is $4m$. However the calculated phase φ using f_1 yields 45° or 216° for f_2. This results in measured distance d of 25 cm or 1.5 m. Of course also the other solutions residing in multiples of the unambiguity range are possible. Therefore both results are combined in order to calculate the true distance. This is achieved by exploiting the fact that only one common possible location exist. It can be evaluated by adding the unambiguity ranges to the calculated distances for f_1 and f_2 until both sums yield the same result. By using this simple method the overall unambiguity range extends according to Equation 2.8 below [PJD+09].

$$d_{u,extended} = \frac{c}{2 \cdot |f_1 - f_2|} \tag{2.8}$$

The relative contribution of both distance measurements can be adjusted using a fixed weighting of 50%. It is also possible that a variable weighting is applied based on the relative signal magnitudes and frequencies of these two distinct measurements. Equation 2.9 shows a possible way of achieving this. A_1 and A_2 are the calculated magnitudes while f_1 and f_2 denote the used modulation frequencies from the two phase frames [JCPD10].

$$d_{weighted} = d_1 \frac{A_1 f_{M1}}{A_1 f_{M1} + A_2 f_{M2}} + d_2 \frac{A_2 f_{M2}}{A_1 f_{M1} + A_2 f_{M2}} \tag{2.9}$$

However this measurement approach yields a disadvantage concerning time-consumption. Four additional phase-frame captures are necessary in order to establish a second measurement utilizing another modulation frequency. To keep a certain acquisition time it is possible to lower the integration times of the PMD pixels. On the other hand this approach reduces measurement accuracy [JCPD10].

2.2.2 Photonic Mixing Device

The correlation-functionality mentioned in Section 2.2.1 is implemented inside the PMD pixels by means of fully analog operation. Therefore there is no need for an additional analog mixing circuit for phase-calculation. Additionally the post-processing effort is reduced as only the arctan function calculations and subsequent error-corrections have to be done by the application processor afterwards.

In order to provide this analog functionality the pixel collects electrons which are a result of incoming photons. A more detailed overview of the device operation is given by figure 2.5. However an intuitive explanation of the basic 4-phase operation is provided by figure 2.4 below. It can be seen that the resulting electrons are accumulated in the pixel during the so-called integration time. This is the time in which the scene is actively illuminated by IR light. The modulation frequency in modern devices is set to be between 20 MHz and 100 MHz. As a consequence integration takes place over multiple thousand periods, because only a few electrons are produced during one modulation period. Therefore long integration times increase the magnitude of the read-out voltage and the SNR. However the pixels can saturate if this is done for too long and the information contained in the read-out voltage cannot be used anymore. The gray areas in figure 2.4 show the time in which light enters the pixel and the respective control signal CS is active. The state of CS depends on the current phase-shift. It is shown separately as $CS0$, $CS1$, $CS2$ and $CS3$ referring to an operation with 0°, 90°, 180° and 270°.

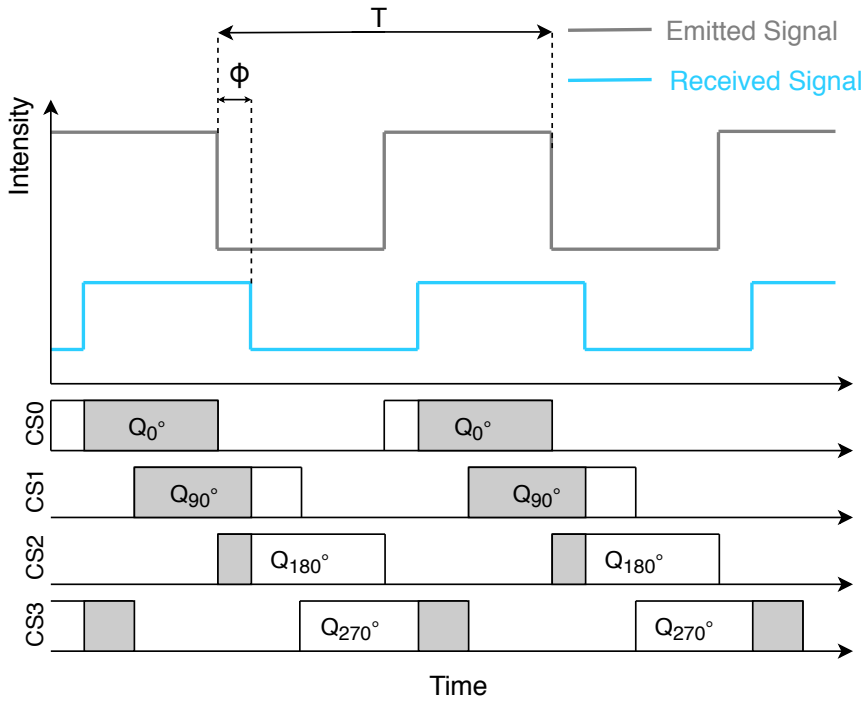

Figure 2.4: Four-phase integration operation of the PMD device. Obtained with changes from [HLCH12].

The PMD establishes three important operations during integration time. Photons are converted into electron-hole pairs, subsequent accumulation of these resulting electrons is done and a multiplication is performed. Conversion is based on the inner photo-electric effect described by Einstein in [Ein65]. Realization of the device is done in standard Complementary Metal-oxide semiconductor (CMOS) technology. The charge transfer mechanism is comparable to well-known CCD's. Two conductive and transparent MOS photogates form the optical sensitive zone of the PMD capable of receiving the CW modulated light emission. Next to them two reverse-biased diodes are located in order to provide charge-sensing capability. Their common anodes are connected to the ground potential [Lua01].

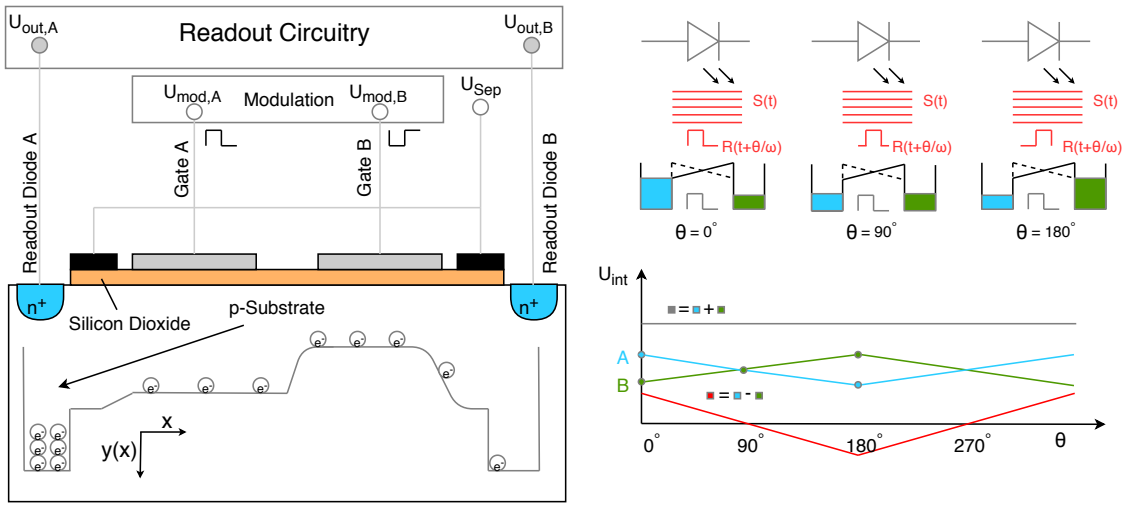

Figure 2.5: PMD device working principle. Schematic of the pixel circuit and sampling of cross-correlation function. Obtained with changes from [Pla06].

The photo gate's are essentially MOS capacitors which can be in accumulation, depletion or inversion state depending on the applied voltages [SN06]. If the photo gate's node voltages are at constant positive DC level a depletion area is formed underneath it. Majority carriers(holes) are pushed into the p-substrate and electrons drift to the surface. However the PMD operates in deep depletion mode which is established by the applied high-frequency modulation signal. Minority carriers are not able to follow the constant changes and therefore the devices stays in non-equilibrium state during operation. Photo-generated electrons are then collected in the space-charge region below the respective modulation gates [Lua01]. Due to the constantly changing terminal voltages the potential gradient in the device also changes synchronously. Generated electrons are as a result either driven into the right or left direction. A measurable voltage is present at the read-out diode terminals because of the accumulated charge in the capacity below them. This voltage approximates the cross-correlation function of the emitted optical signal $S(t)$ with a phase-shifted sampling signal $R(t)$ [Pla06]. The sampling of the respective correlation functions are shown in figure 2.5.

The above described mixing operation is achieved by applying a differential modulation signal at the terminals $U_{mod,A}$ and $U_{mod,B}$ respectively. Hence these modulation gate voltages are contrary to each other. In practical realizations they do not employ a

sinusoidal but rather a rectangular-like shaped form. The reason lies within the easier on-chip voltage-generation of phase-shifted rectangular waveforms and because of the more efficient operation of the VCSEL light-source.

During measurement the PMD undergoes different phases. The device operation is therefore split up in Reset-, Integration- and Readout-Phase. In order to operate the pixel within different phases typically a 4-transistor architecture is used. A possible realization of such a circuit is presented in figure 2.6 which also exhibits the integration-voltage V_{int} over time for two cases of operation. Every pixel incorporates this circuit two times. This is due to its differential structure as it is shown in figure 2.5.

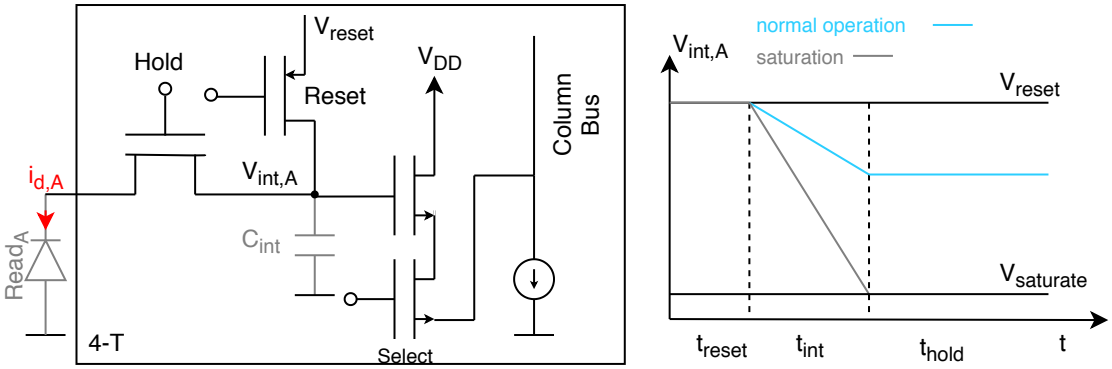

Figure 2.6: A possible realization of a 4-T read-out architecture and phases of operation during exposure time. Obtained with changes from [vVGK06].

- In the **reset** phase the voltage drop over C_{int} is set to V_{reset}. In order to achieve this the hold- and reset-transistor are closed. C_{int} is therefore pre-charged to a defined voltage level.

- During **integration** time the reset-transistor is opened and the hold-transistor is closed. A current-flow between the C_{int} and read-out diode takes place. This current denotes the photo-current generated by the PMD. Due to the resulting charge-transfer the voltage level V_{int} drops during exposure. However there is a voltage-limit $V_{saturate}$ which marks the wanted range of device-operation. If the integration-voltage hits this boundary an unwanted saturation-state of the device is reached.

- Throughout the **readout** phase the hold-switch is opened. Also the reset-line is disconnected from C_{int}. The respective select transistor is turned on. This establishes a connection between the second transistor above it and the current-source on the column bus. Together they form a source-follower circuit which acts as a voltage buffer for the subsequently connected ADC circuit. In practical realizations several pixel-groups are physically linked to one ADC. The voltage-level is kept constant until the next reset-phase which pre-charges the capacitor again.

2.2.2.1 SBI circuit

The saturation effect described in the previous section is mainly caused by uncorrelated background light(e.g: sunlight). In order to provide a prevention mechanism a so-called Suppression of Background Illumination (SBI) circuit is present for every pixel. Uncorrelated light results in the same amount of charge-carriers collected in both of the read-out capacities. Therefore it only leads to an increase of the DC level and does not add usable information [Sch05].

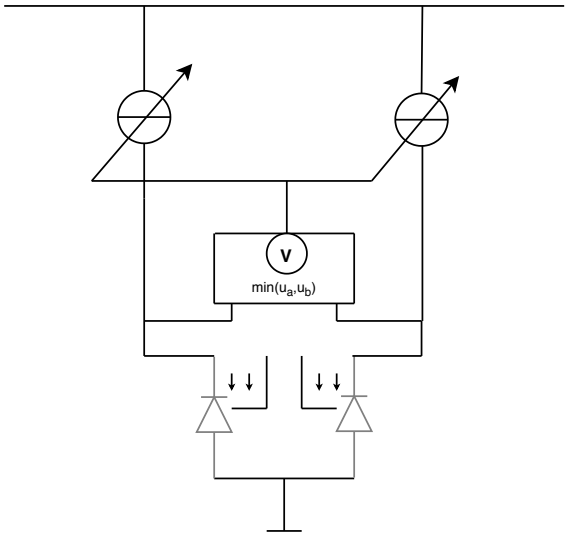

Figure 2.7: Simplified schematic of SBI circuit. Obtained with changes from [Sch05].

During device operation the correlation voltages at the read-out capacitors are constantly monitored. Utilizing these measured voltages, the corresponding photo-currents of the read-out branches are calculated. The smaller current of these two is now injected in the opposite direction with respect to the photo-current. This is applied in both branches and leads to preserving the voltage-difference while reducing the DC level of the PMD. By applying this method not only the uncorrelated background light is compensated, but also the DC voltage caused by the non-ideal separation of charge-carriers is canceled out. On the other hand the sampled phase-image does not represent the gray-scale image, but rather shows the infrared reflectivity of the scene [Sch05].

2.2.2.2 Demodulation contrast

The demodulation contrast is a characteristic of the mixing process inside the PMD. It is also known as demodulation efficiency and describes the ratio between successfully separated charge-carriers and the overall generated number of charges inside the device. By summing up the integration voltages U_A and U_B and calculating the difference this can be established easily. The DC contrast is defined in Equation 2.10 below [Alb07].

$$K_{DC} = \frac{|u_{int,A} - u_{int,B}|}{u_{int,A} + u_{int,B}} \cdot 100\% \tag{2.10}$$

In practical implementations the measurement is carried out using different phase-shifts for the modulation. Now the contrast can be determined for each of them separately. The highest possible separation is observed by utilizing a phase-shift of $\varphi_{ToF} = 0°$ or $\varphi_{ToF} = 180°$ respectively. This is because the photo-currents in both read-out branches have their maximum dissimilarity. Subsequently the contrast is determined by measuring the demodulation efficiency at those two positions of the cross-correlation function and averaging the result. The overall modulation contrast is further determined using Equation 2.11 [Alb07] .

$$\begin{aligned} K_{0°} &= \frac{|u_{int,A}(\varphi = 0°) - u_{int,B}(\varphi = 0°)|}{u_{int,A}(\varphi = 0°) + u_{int,B}(\varphi = 0°)} \cdot 100\% \\ K_{180°} &= \frac{|u_{int,A}(\varphi = 180°) - u_{int,B}(\varphi = 180°)|}{u_{int,A}(\varphi = 180°) + u_{int,B}(\varphi = 180°)} \cdot 100\% \\ \implies K &= \frac{1}{2} \cdot (K_{0°} + K_{180°}) \end{aligned} \tag{2.11}$$

2.2.2.3 Fill factor

The photo-sensitive area of a PMD does not cover the whole pixel. As a measure for the yield the relation between overall and photo-sensitive area is called the fill-factor. Read-out diodes have to be covered in order to prevent the generation of uncorrelated charges in the device. Additionally there are electrical connections to the pixels and transistors which require surface area. There exist different solutions in order to enlarge the sensitive area. Using an architecture which shares read-out transistors is one possible example. Another way of ensuring more usable surface is utilizing back-side illumination. As a consequence read-out circuits do not influence the sensitive are, because they reside in front of the pixel. Micro-lenses are also used to increase the fill-factor by focusing incoming light on the photo-sensitive area [BBMP10].

2.2.2.4 Spectral photoresponse

Describes the relation between the received optical power P_{opt} and the resulting photo-current i_{photo}. It is defined according to Equation 2.12 [JHG99a].

$$R_s(\lambda) = \frac{i_{photo}}{P_{opt}(\lambda)}[A/W] \tag{2.12}$$

It is visible that this ratio depends on the wavelength emitted by the light-source. In order to determine this value a PMD without read-out circuit is illuminated at a specific

wavelength while measuring the emitted optical power using a photo-diode. The resulting photo-current can be directly calculated by measuring the respective integration-voltages. However, this also incorporates the impact of process variation of the integration capacities and yields errors depending on these influences. The direct current-measurement does provide better results, but introduces the need of high-precision measurement devices [Alb07].

2.2.2.5 Quantum Efficiency

Quantum efficiency is a measure to asses the conversion-process of photons into electron hole-pairs inside the PMD. The maximum value which can be reached is 1. This results in an electron-hole pair for each arriving photon. However, this ratio diverts in practical implementations. The reason lies in recombination and possible reflections. The formal definition of quantum efficiency is given in Equation 2.13 [ZZ10].

$$\eta_{ex} = \frac{N_{e^-}}{N_{Photon}} = \frac{i_{photo}/e^-}{P_{Opt}/(h \cdot v)} \tag{2.13}$$

2.3 Errors in ToF measurements

There exist two main sources of errors in ToF imaging using the PMD measurement technique. They can be categorized in systematic and random errors. In the following sections an explanation of the various error sources is given.

2.3.1 Systematic Errors

Systematic errors are caused by the system's non-ideal behavior when applying the proposed measurement procedure. They are temporal independent and can be considered constant during operation. Calibration techniques have been developed in order to mitigate them. In the following sections their nature is explained.

2.3.1.1 Wiggling Error

The depth-calculation utilizing CW modulation explained in Section 2.2.1 is based on the assumption of sinusoidal illumination and modulation. Hence the *atan* calculation is only valid if sinusoids are employed. In practical realization this is not the case. As a consequence a so-called circular distance error is introduced in the measurement. This phenomenon is described as wiggling-error in literature and is shown in figure 2.8 below.

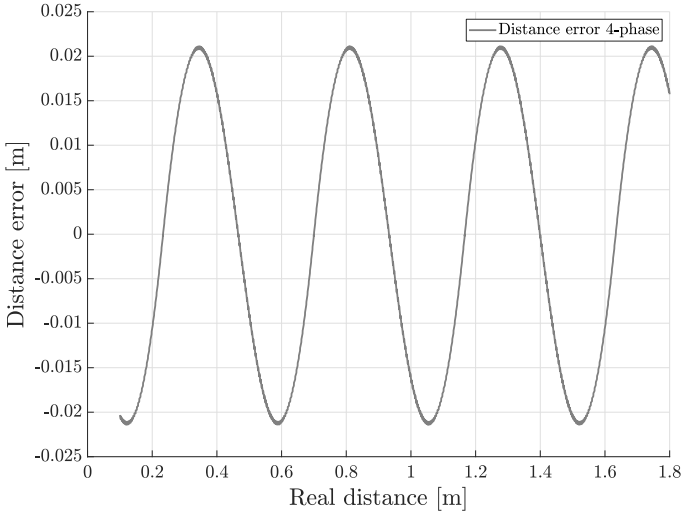

Figure 2.8: Circular distance error in ToF measurement.

The amplitude of this error is highly dependent on the distance between scene and sensor. Furthermore it is influenced by the waveform of the illumination and modulation signal. In figure 2.8 above rectangular-shaped waveforms were used for both signals. However this does not reflect reality as rectangular waveforms cannot be realized, but it is sufficient to show the nature of the error.

In order to overcome this error extensive calibration techniques are applied. This has to be done separately for every device [LKR08]. Another possible way to reduce this error is to employ an odd number of phase images for calculation [Gru13].

2.3.1.2 Amplitude-related error

The true origin of this error is believed to be the non-linear behavior of the pixel and read-out circuitry. If different materials are illuminated by the sensor system the amount of arriving photons depend on the reflection/absorption properties of the specific material. Dark surfaces absorb more light and less photons arrive back at the photo-sensitive area. This results in a weaker signal sensed by the sensor-core. Due to a non-linear transfer function of the system subsequent errors in distance calculations can be observed. Figure 2.9 below shows the depth deviation due to varying reflectivity of a checker-board pattern.

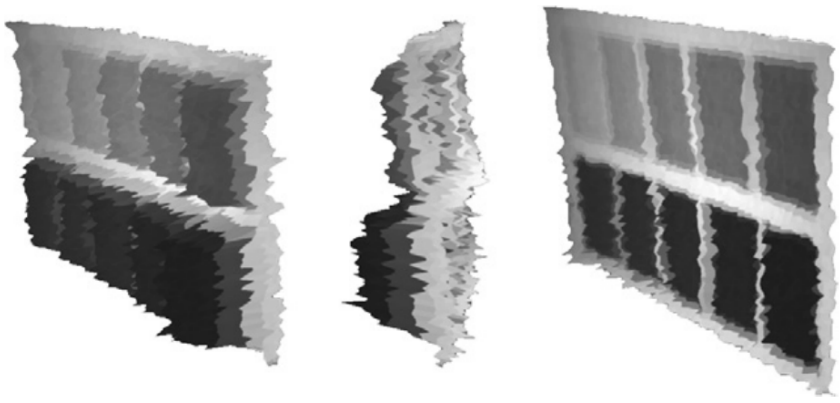

Figure 2.9: Depth deviations due to varying reflectivity of the object [LSKK10].

2.3.1.3 Fixed-pattern noise

Fixed Pattern Noise (FPN) is a pixel-dependent spatial error and does not have noise properties due to its constant behavior in a fixed environment. It shows itself as an individual offset and a multiplicative deviation, also called Photo-response non-uniformity (PRNU) added to an intensity-image. This is mainly caused by manufacturing variations [Alb07].

Read-out of the pixels is done by using column-amplifiers incorporating current-sources with varying properties. The transistor involved in resetting the PMD also introduces variations. Additionally the ADC's embedded into the sensor itself have varying DC errors. These deviations add up and result into the previous described error. By inspecting variations across the image-sensor, a column-wise structure can be observed. This is caused by the architecture of the read-out circuit, mainly by the column-arranged amplifiers. Pixels in the same column also have varying electrical paths resulting in different common-mode voltages of U_a and U_b respectively. Due to the subsequent differential read-out and symmetrical properties of the branches A and B this offset is canceled out though [Alb07].

In order to correct the introduced deviation a so-called dark-frame using a minimum exposure-time and a disabled illumination is captured. This eliminates the dependency of the measurement regarding optical emission power and dark current. Subsequently the frame can be stored in a LUT, because of its constant nature. By simply subtracting the gathered frame a correction removing the FPN can be achieved. Figure 2.10 below shows a captured dark-frame using an Infineon IRS1645 ToF sensor clearly incorporating column-wise visual stripes. The gray-scale visualization is established by setting the minimum measured LSB count as lower-boundary and the maximum observed LSB count as upper-boundary respectively.

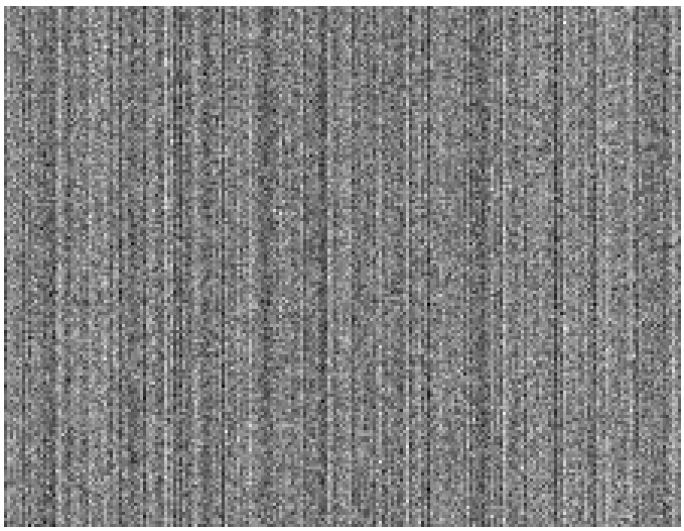

Figure 2.10: Dark-Frame showing the effect of FPN.

2.3.1.4 Fixed pattern phase noise

FPPN describes a similar error compared to the FPN. It also does not employ noise and is constant. Additionally to an offset voltage there is a fixed individual phase-offset which adds up to the measured phase for every pixel. Routing of the respective modulation voltage U_{mod} is done utilizing a tree-structure to keep the path distance to each pixel as similar as possible. Nevertheless the resistance and also the traveling time seen by the modulation signal along a column adds-up as previously described in Section 2.3.1.3. This circumstance does not sufficiently describe the observed phase-offset though. Utilizing a High-Frequency (HF) equivalent circuit diagram described by the serial connection of several passive RC-circuits the error can be modeled [Alb07].

2.3.2 Noise sources

Errors caused by noise-sources do employ temporal dependence and can only be described by utilizing statistics. This is necessary, because an exact definition cannot be given due to lack of knowledge beforehand. The following sections describe the most important random error sources and their overall contribution to the measurement.

2.3.2.1 Reset-Noise

This error-source, also called kTC-noise is the uncertainty of charges accumulated in the integration capacity after the reset-phase of the measurement established by the reset transistor. It is described using Equation 2.14 and 2.15 and is caused by thermal noise which is outlined in section 2.3.2.4 [JHG99b].

$$\Delta Q_{kTC} = \sqrt{k \cdot T \cdot C_{int}} \tag{2.14}$$

$$\sigma_{kTC} = \frac{\Delta Q_{kTC}}{e^-} = \frac{\sqrt{k \cdot T \cdot C_{int}}}{e^-} \tag{2.15}$$

ΔQ_{kTC} is given in charges accumulated in the integration capacity and σ_{kTC}'s unit is number of charges. k is the Boltzmann constant and T the absolute temperature.

2.3.2.2 Photon shot-noise

Photon shot-noise describes the uncertainty of photons arriving at the image sensor. Additionally it involves the electrons-hole pairs generations inside the device. Exact time of arrival and emission of a single photon utilizing a continuous, homogeneous light-source cannot be determined. This is due to unforeseeable variations and can be described using a Poisson distribution. The photon shot-noise is further determined by calculating the standard-deviation of the number of photo-generated charge-carriers. This is shown in Equation 2.16 [Jah09].

$$\sigma_{noise,shot} = \sqrt{N_{e^-}} = \sqrt{\frac{Q_{e^-}}{e^-}} \tag{2.16}$$

$\sigma_{noise,shot}$ describes the standard deviation given in number of charge-carriers. N_{e^-} is the amount of the overall photo-generated charges. Q_{e^-} is the overall charge.

2.3.2.3 Dark current and dark current shot-noise

The PMD does not only accumulate charges due to arriving photons. Because of thermal oscillations which are independent of incoming light, electrons are additionally created. This results in the dark current i_{dark} which can be described by the Boltzmann distribution. The average dark current can be determined by subsequent measurements and subtracted afterwards. However, the true origin is stochastic and therefore the dark current shot-noise cannot be compensated and is described by Equation 2.17 below [Jah09].

$$\sigma_{dark} = \sqrt{N_{e^-,dark}} = \sqrt{\frac{i_{dark}}{e^-} \cdot T_{int}} \tag{2.17}$$

2.3.2.4 Thermal noise

Thermal noise describes the statistical, omni-directional movement of free charge-carriers in a semiconductor due to thermal noise. Equations 2.18 and 2.19 shows the resulting voltage and current [Jah09].

$$u_{therm,rms} = \sqrt{4 \cdot k \cdot T \cdot R \cdot \Delta f} \tag{2.18}$$

$$i_{therm,rms} = \sqrt{4 \cdot k \cdot T \cdot G \cdot \Delta f} \tag{2.19}$$

$u_{therm,rms}$ and $i_{therm,rms}$ describes the effective noise voltage and current. R is the resistance and G the conductance while Δf describes the bandwidth.

2.3.2.5 Quantization noise

Analog signals are usually converted in discrete numerical values in order to be post-processed. Therefore a so-called quantization error is introduced in the measurement. This is also the case in evaluating integration voltages of the PMD pixels. The quantization error is uniformly distributed between $-\frac{1}{2}LSB$ and $+\frac{1}{2}LSB$ and describes the deviation from the actual input voltage. In current implementations the resolution is $12-bit$ utilizing Successive Approximation Register (SAR) based ADC's. The minimum voltage-step which can be sensed by the converter is determined by the Equation 2.20. Equation 2.21 describes the standard deviation of the conversion.

$$u_{LSB} = \frac{u_{range}}{2^{N_{bit}}} \tag{2.20}$$

$$\sigma_{adc} = \frac{u_{LSB}}{\sqrt{N_{bit}}} \tag{2.21}$$

u_{range} determines the input voltage range and N_{bit} the numbers of bits of the converted digital word.

2.3.2.6 Photon Transfer Curve

In order to quantify the impact of the various described noise-sources it is beneficial to investigate them in dependence on the observed light intensity. Figure 2.11 shows them in a logarithmic scale. In low-light conditions the read-out noise is dominant over the photon shot-noise. This noise-source consists of a combination of reset-noise and dark-current shot-noise as well as others. It is added as a constant to the photon transfer curve [Jah09].

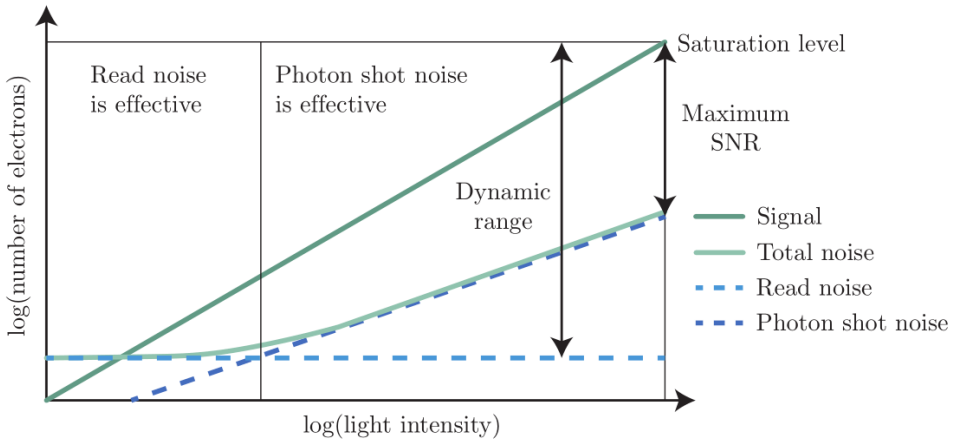

Figure 2.11: Noise-sources in dependence on light intensity [All18].

As the light intensity increases photon-shot noise becomes more dominant. This error-source cannot be eliminated and directly relates to the maximum possible SNR. The image sensor's dynamic range is given by the minimum amount of light required in order to sense a signal and the maximum number of charges which can be accumulated before a saturation state is reached [Lan06].

2.4 State of the Art

The following sections describe the state of the art in the field of this thesis. It explains some of today's various applications of Mobile Phone Sensing. Subsequently proximity sensing in the context of mobile applications is examined concluding with existing 3D ToF approaches.

2.4.1 Mobile Phone Sensing

Mobile phones play a central role in modern human life. According to a forecast of November 2016 found in [Depa] there are now 4.68 billion users world-wide. By 2020 this number is predicted to grow beyond 5 billions. Due to continuous improvement in System-on-Chip (SoC) technology these devices are even capable of replacing desktop PC's for certain applications. In the U.S. the percentage of people owning a cellphone(including smartphones) has outgrown desktop/laptop computer owners. As reported by [Cen] 92% of U.S. adults own cellphones and only 73% a desktop or laptop computer. Mobile phones are also one of the main-causes of nowaday's internet traffic. 52.2% of all web pages visit's were made using mobile phones as stated in [Depb].

In contrast to typical desktop PC's smartphones contain a growing number of sensors to perceive the environment and track the user's behavior. Even an entry-level phone incorporates embedded sensors such as accelerometer, gyroscope, GPS, ambient-light, proximity

and at minimum two cameras. With growing numbers of sensors also new applications emerged. The survey described in [LML+10] was conducted in the early year of 2010 examined the development of sensors and resulting applications in smartphones. They classified them in the following categories

- **Transportation**

  Mobile phone sensing systems help to provide detailed traffic information in order to improve travel time estimation and subsequent commute planning. Such services are already included in Google Maps and other navigation-based applications.

- **Social Networking**

  Social Networks are used by billions of people everyday. Events in people's live can be automatically captured using the build-in sensors present in a smartphone and shared on social networks such as Twitter or Facebook.

- **Environmental Monitoring**

  Measuring and reporting changes of environmental conditions(e.g: air pollution) are build on aggregate statistics which apply for a whole area or city. The project described in [MRS+09] incorporates sensor data of phones to provide a way for users to create their own personal environmental impact report. As a consequence they are able to track how actions of them influence the exposure and contribution to certain problems(e.g.: carbon emissions) [LML+10].

- **Health and Well Being**

  Most of the information in personal health care are generated by self-report surveys and rare discussions with a doctor. Smartphones are capable of continuously collecting sensor data(e.g: accelerometer, gyroscope) which can be used to evaluate health and well-being as well as care and treatment of the patient. The project described in [CMT+08] collects levels of physical activity and compares it to the personal health goals set by the user and provides feedback. These systems have proven effective in motivating people to establish a healthier lifestyle and reduce poor behavior patterns [LML+10].

A more recent survey embeds mobile sensing in pervasive health-care. It shows that continuous capturing of smartphone sensor data is already implemented in some of today's health-care frameworks. Their findings are reported in [TVS+17].

Another major field involving Mobile Phone Sensing is the Internet of Things (IoT). Since smartphones are highly integrated in networks their collected sensor data can be effectively shared among other handheld devices or stored in the cloud. This offers the opportunity to create platforms which fuse the information in order to provide improved services. One example of such a system is shown in [BP17].

2.4.2 Proximity Sensing in Mobile Applications

Proximity sensing describes the ability to detect the presence of one or several objects without direct contact. There exist various measurement techniques based on different physical effects. Due to its broad definition research work in this area reaches from industrial safety applications to networked sensors and sensor fusion as it is shown in [KKC19]. However, in this section optical proximity sensors incorporated in modern mobile devices will be examined regarding their architecture and measurement principle. Their main purpose is usually to detect a nearby head in order to signal the phone processor to shut-down the display while the user is having a phone call.

2.4.2.1 Intensity based

Intensity-based proximity sensors mainly consist of a light-source and a photo-diode. Additionally a narrow-band optical filter is usually attached in front of the proximity-measurement related photo-diode. This filter is designed to attenuate unnecessary ambient light-components. These types of systems are not able to directly gather distance information with high-resolution. Instead only an intensity-level of reflection is provided in order to detect the presence of an object. Often an additional ambient light sensor is incorporated to increase value for the device manufacturer.

An example of an implementation is explained in [SFS+16]. This solution focuses on a medical application, namely blood oximetry monitoring and heart rate measurement. Nevertheless it is additionally capable of operating as a traditional proximity and ambient light sensor. Therefore it is also based on measuring the intensity of reflected invisible light emitted by a constant light-source (e.g.: IR-LED). However, this system only uses a single photo-diode for both proximity and ambient-light sensing. Therefore the optical filter is designed to have a broad pass-band. As a consequence the photo-diode senses a large amount of ambient-light. A second measurement with disabled illumination would be necessary to subtract this component when doing proximity sensing. The solution proposed in the above mentioned paper uses a modulated light-source and a synchronous demodulation receiver which inherently rejects background illumination. As a consequence only the amplitude of the pulsing component is aquired. This ensures full dynamic range of the sensor even in the presence of a bright background illumination. Ambient light measurement is further done by just evaluating the intensity measured by the embedded photo-diode without actively illuminating the scene.

Figure 2.12 shows the block diagram of the described sensor system. The signal path containing an AC-coupled TIA, a two-stage dc-rejection circuit and a Delta-Sigma ADC are able to operate with at least 13.2 bit ENOB.

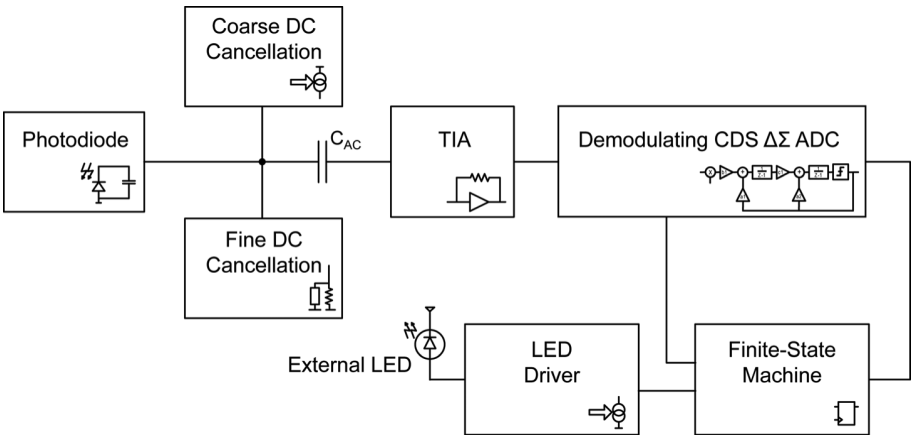

Figure 2.12: Block diagram of the combined system utilizing proximity- and ambient-light sensor functionality [SFS+16].

2.4.2.2 SPAD based

Another sensor architecture used in mobile proximity sensing is based on Single-photon avalanche diode (SPAD) devices. Due to recent developments in miniaturizing these systems even implementations of whole pixel arrays became possible. Several sensor manufacturers including STMicroelectronics and ams are offering sensors utilizing SPADs suitable for smartphones and other mobile devices.

Its measurement principle can be classified as direct ToF, because the arrival-time of incoming photons emitted by a laser light-source is directly evaluated by a Time-to-digital converter (TDC). The solid-state photo-detector is based on a pn-junction which is reverse-biased exceeding the break-down voltage of the junction. Therefore the electrical field inside the device reaches a level wherein a single photo-generated electron in the depletion layer triggers a self-sustaining avalanche. As a result the current rises within nanoseconds to a steady mA level. This pulse marks the arrival of the incoming photon and can be used to subsequently measure the time-delay and distance to an object. Afterwards it is necessary to quench the current by biasing the pn-junction below or equal to the break-down voltage. Restoring of the device is done by setting the operating voltage well above the break-down voltage again [CGL+96].

Figure 2.13 shows the described avalanche events over time happening in a SPAD device fabricated in 28nm CMOS process. The corresponding implementation described in [dCC+18] integrates the SPAD below the buried oxide with control logic residing on-top in the thin silicon layer. This ensures a large fill-factor.

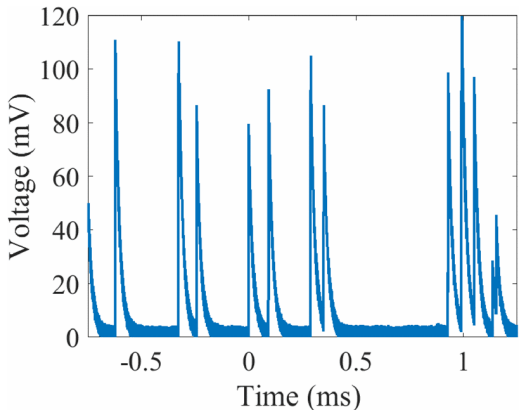

Figure 2.13: Avalanche events in a SPAD device [dCC+18].

An early implementation in 2017 based on the above described architecture is reported in [VCR17]. It shows the first successfully manufactured 64x64 SPAD pixel array in a standard CMOS process. Utilizing this system even 3D image capturing within a distance resolution of 1 cm is possible. As a drawback it is not suitable for mobile devices due to its size. Another realization of a SPAD array focusing on Unmanned Aerial Vehicle (UAV) applications is described in [SP18]. The authors are stating that this system is capable of measuring distances up to 300 m.

However, there already exist miniaturized SPAD sensors suitable for mobile applications. The ams TMF8701 is a recently developed ToF sensor which incorporates a single SPAD. It offers proximity sensing functionality and can be integrated in smartphones. Figure 2.14 shows a simplified block diagram of a typical system. Another recently developed SPAD based sensor with small footprint is the ST VL53L. It can be used within a range of up to 4 m. There already exist a paper describing the usability of this sensor towards robot environment detection. The detailed findings are reported in [LBB+19].

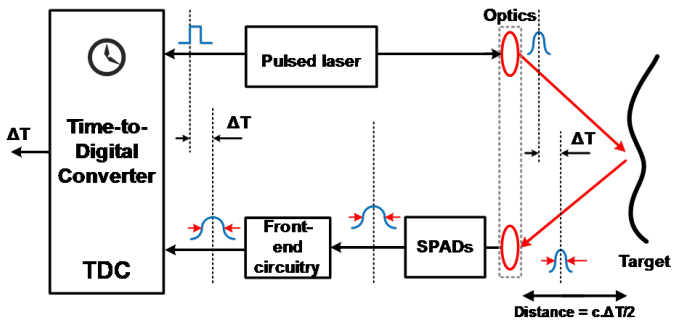

Figure 2.14: Simplified block diagram of a typical SPAD-based system [Lab].

2.4.2.3 PMD based

PMD based ToF cameras are also an architecture found in some modern smartphones(e.g: LG G8). The measurement principle is extensively described in previous Section 2.2.1.

Main applications are face- and gesture-recognition. 3D images can be created yielding high resolution results within several meters. Low-power modes with limited performance comparable to the existing previously described architectures are currently not available which disqualifies them for proximity sensing purposes. Therefore an additional sensor has to be present to provide this functionality.

2.4.2.4 Specifications of commercial proximity sensors

Several commercial proximity sensors were investigated regarding their specifications. The respective datasheets were collected and important parameters were extracted. Table 2.1 incorporates these values of interest. All of the below mentioned devices are either intensity-based or SPAD based architectures. The supply voltage range is shown as well as the typical operating voltages which were applied while measuring the current. Unfortunately device manufacturers are specifying the power consumption while operating on different measurement frequencies. Thus the Table 2.1 below additionally shows the refresh period belonging to the specified current consumption. The maximum measurement frequency of the devices can be derived from the minimum readout period on the far-right column in the table below.

Model	**FoV**[°]	**Power[mW]**	**Range[m]**	**Readout[ms]**
Broadcom APDS-9160	30	1.54 @ 100ms	0.07	6.25
Infineon PALS-2	n.a.	0.8 @ 125ms	0.3	4
Vishay VCNL4035x01	30	0.5 @ 7.81ms	0.2	7.81
ST VL53L1X	27	44.8 @ 33ms	4	33
ST VL6180X	n.a.	4.76 @ 100ms	0.1	15
OnSemi NOA3301	30	0.495 @ 100ms	0.1	5
ams TMF8701	21	3.102 @ 100ms	0.6	16

Table 2.1: Specifications of commercial proximity sensors used in mobile devices.

It is visible that intensity-based proximity sensors do have the lowest power consumption. This is mainly caused due to the illumination light-source which is designed for low-range sensing. Examples of such architectures are the Broadcom APDS-9160, Infineon PALS-2 or the OnSemi NOA3301. Their power-consumption is below 1 mW of course varying depending on the measurement frequency. SPAD based systems like the ST VL53L1X or ams TF8701 employ laser diodes in order to extend the range and resolution of the measurement. Additionally these sensors incorporate circuits for operation of the SPAD device which need a high-precision control-system, a TDC and even a microprocessor in some implementations. All these components add up to an overall increased power-consumption. The ST VL53L1X is the most power-demanding system using up to $44.8mW$ while operating at maximum readout period of 33 ms.

Chapter 3

Design

This chapter describes the conventional measurement architecture regarding ToF systems. It explains the processing and calibration pipeline commonly used in order to create high-accuracy depth-images. Furthermore the drawbacks of this approach is explained regarding power consumption and usability for proximity sensing. Subsequently a new processing pipeline is presented. In order to establish this new approach the systematic errors involved in the measurement are examined. Therefore an existing simulation model was extended. Additionally a software for the evaluation of real ToF sensor data was created.

3.1 Conventional ToF Processing

In Section 2.2.1 the basic algorithm for ToF 3D image creation is explained. Practical realizations additionally employ correction steps which have to be implemented to increase measurement accuracy. The result is a processing pipeline consisting of several steps which are applied subsequently. Figure 3.1 shows the processing steps.

At the beginning four phase images are captured and pixel data is collected. This data stream is then further processed by extracting only data of active pixels and storing them in an appropriate structure. All the phase images are checked for a saturation condition. If one of the images is saturated the exposure-time is adjusted and measurement is carried out again. After that an optional stray light correction is applied. Now the depth-calculation is done by evaluating equation 2.3 shown in Section 2.2.1.1. Due to the influence of the systematic wiggling-error a phase-dependent correction is applied by interpolating between values stored in a LUT. Based on the gathered phase-values a depth image is created which is further temperature compensated and filtered. The noise filter adjusts its parameters by inspecting an intensity-image which is captured at the end of the measurement sequence. This so called gray-image has to be FPN corrected in order to provide intensity information. Finally the filtered depth-image can be up-sampled by interpolating between the discretely arranged pixels. This results in a fine-grained point-cloud which can be used by the application.

The above described procedure is often extended by operating the sensor with a different modulation frequency. As a consequence the range of unambiguous measurement results is increased, but all the processing steps have to be done twice and result in eight phase-images and one gray-image which are captured and processed within one depth frame.

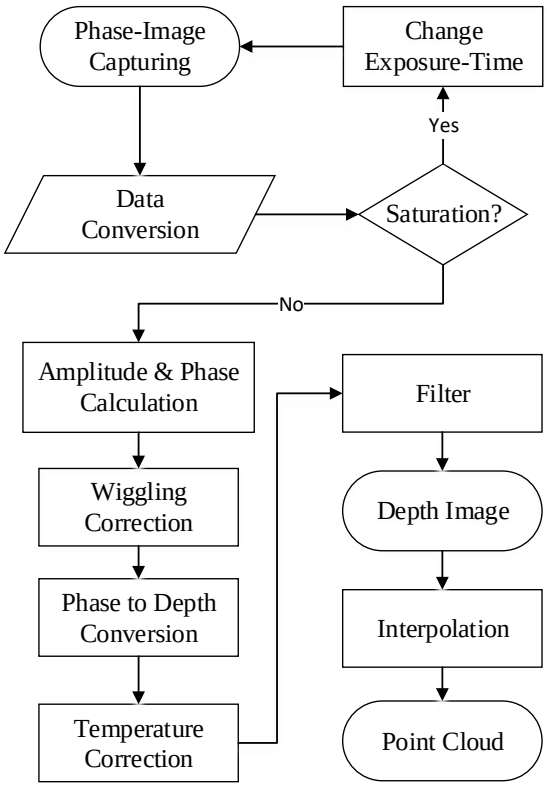

Figure 3.1: Current ToF processing steps for depth calculation.

3.1.1 Limitations

The described processing in Figure 3.1 provides high-accuracy depth maps of the environment. However, several phase images are required in order to achieve this. Every raw-phase except of the gray-image requires active illumination. Additionally a large amount of raw-data has to be transferred to the application processor. Therefore power- and time-consumption is increased which makes this approach inappropriate considering proximity-sensing functionality.

3.1.2 Power Profile

A ToF sensor system incorporates several components which require different current consumption for varying use-cases depending on several factors. The power required by the sensor and illumination add up to an overall power profile. As explained in section 2.2.2 the sensor undergoes capture, readout and idle phases during measurement. The current consumption varies depending on these states and has to be expressed as an average for the whole period of phase image capturing.

Table 3.1 below shows three different sensor use-cases operated with differing frame-rates and exposure-times. It is valid for the current sensor implementation utilizing a $2W$ VCSEL as a light-source. The naming of the use-cases follows the number of included phase-images inside one measurement. The table incorporates the required energy during the different measurement states in mJ. In order to calculate the overall power consumption the accumulated energies are divided by the inverse of the Frames Per Second (FPS).

Use Case	FPS	t_{exp}[ms]	Capture[mJ]	Readout[mJ]	Idle[mJ]	**Overall[mW]**
Mode 2	1	0.1	0.058	0.689	9.911	**10.66**
Mode 5	1	0.1	0.192	1.721	9.892	**11.8**
Mode 9	1	0.1	0.37	3.099	9.866	**13.33**
Mode 2	3	0.1	0.058	0.689	3.295	**12.12**
Mode 5	3	0.1	0.192	1.721	3.276	**15.57**
Mode 9	3	0.1	0.37	3.1	3.25	**20.16**
Mode 2	1	0.5	0.29	0.689	9.9	**10.88**
Mode 5	1	0,5	0.96	1.721	9.871	**12.55**
Mode 9	1	0,5	1.851	3.099	9.83	**14.78**
Mode 2	3	0.5	0.29	0.689	3.287	**12.8**
Mode 5	3	0.5	0.96	1.721	3.256	**17.81**
Mode 9	3	0.5	1.851	3.099	3.214	**24.49**
Mode 2	1	1.0	0,58	0,689	9,893	**11.16**
Mode 5	1	1.0	1.918	1.721	9.847	**13.49**
Mode 9	1	1.0	3.702	3.099	9.786	**16.59**
Mode 2	3	1.0	0.58	0.689	3.277	**13.637**
Mode 5	3	1.0	1.918	1.721	3.231	**20.61**
Mode 9	3	1.0	3.702	3.099	3.17	**29.91**

Table 3.1: Power profiles of various sensor use-cases.

It is visible that the required energy is dominated by the read-out state. This is due to the large time-span in which the sensor is in idle mode when operating at low FPS. The readout energy is determined by the number of phase images inside the use-case. For each of the raw frames the sensor core has to establish a read-out of the pixel voltages and subsequently transfer them using the MIPI interface. As a consequence there is a direct linear relation between the number of raw-frames and the readout energy which is required to gather and transfer them. By comparing the power profiles of the use-cases for $t_{exp} = 0.1ms$ and $t_{exp} = 0.5ms$ it can be seen that they yield similar values. This is due to the dominating energy during the readout in comparison with the capture state when using these short exposure times. Together with the idle state power consumption it marks the lower boundary for the overall power profile. Therefore it is not possible to decrease the power consumption below 10 mW. Further improvements of the energy required during idle times have to be made. Another possibility for power reduction is to implement a partial read-out of the sensor core. This results in fewer active ADCs and current sources. Additionally less data has to be transmitted over the serial connection.

3.2 Simulation Model

Additional improvement and functionality was added to the existing Matlab ToF model which is extensively described in [All18]. Therefore a new ADC model was designed. Furthermore the possibility to add measured illumination waveforms was added by extending the corresponding module. Utilizing the improved simulation environment a more accurate estimation of the impact of systematic errors on the depth measurement could be done. By exploiting the improved simulation results a suitable low-power ToF processing architecture can be found.

3.2.1 ADC

Figure 3.2 shows the connections of the new ADC model describing the differential converter used by the ToF sensor. The ADC quantizes the integration voltages provided by the integrated PMD's for subsequent processing and transmission. This is modeled by a high-level model which is independent of the specific ADC architecture. It only describes the applied conversion process and its effect.

The input parameters of the model determine the overall shape of the ADC's transfer function. By utilizing the values provided by the input channel the model calculates the corresponding discrete digital output words which are further processed by the simulator. Additionally a flag which shows a saturation condition is provided. This can be used to inform the subsequent depth processing about a possible data corruption. As described above several parameters are necessary to adjust the model. They are now explained briefly.

- **Vref**

  This parameter determines the voltage reference which is used by the ADC. It marks the positive and negative boundary of the transfer function.

- **Input**

  Input data is represented using a matrix incorporating the raw values which should be converted. Depending on the algorithm used for depth calculation the size changes accordingly. Furthermore it also depends on the mode in which the simulator is operating (distance-, background light- or integration time-sweep) and the specified distance resolution.

- **N**

  The number of bits used in the conversion is determined by N. By increasing this value the resulting transfer function is more fine-grained. This is due to the quantization interval determined by equation 3.1. Therefore the conversion becomes more accurate and the sigma of the quantization noise decreases as described by equation 2.21.

$$q = \frac{FSR}{2^N}(V/LSB) \tag{3.1}$$

- **Gain**

  A gain error describes the value by which a linear slope connecting positive and negative boundary of the input range is multiplied. Therefore a gain error of zero would result in a multiplier of 1. The definition of the error is given in percentage with respect to the FSR of the ADC. Equation 3.2 below shows the resulting slope incorporating the gain error.

$$k_{gain} = \frac{2^N}{FSR + FSR \cdot error_{gain}}(LSB/V) \tag{3.2}$$

- **Offset**

  If the transfer function does not cross the origin of the axes an offset error is present. Therefore it can be described by a constant added to the linear transfer function. The magnitude of this deviation is expressed in LSB.

- **INL**

  This parameter determines the maximum deviation of the converter from the ideal linear transfer function in LSB. It is determined after eliminating gain and offset error components. The detailed description can be found in section 3.3.1.

- **DNL**

  If the conversion steps do not employ a constant behavior and deviate from $-\frac{q}{2}$ and $+\frac{q}{2}$ a DNL error is present. This input parameter expresses the boundary of the distribution used to model this error source. A detailed description of the error can also be found in the subsequent section 3.3.1.

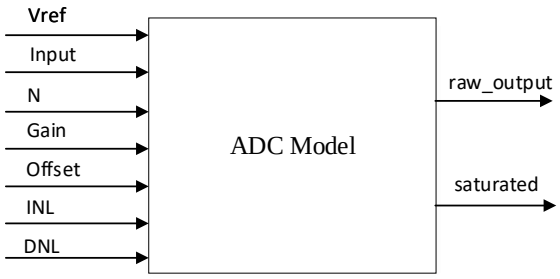

Figure 3.2: Input and output signals of the ADC model.

3.2.2 Illumination Waveform

In order to incorporate the measured illumination signal the corresponding existing module was extended. Therefore the waveform generation functionality was expanded. Figure 3.3 shows the input and output signals of the module which is responsible for this. It is capable to generate both illumination and reference signals used subsequently for calculating the resulting sensor response function.

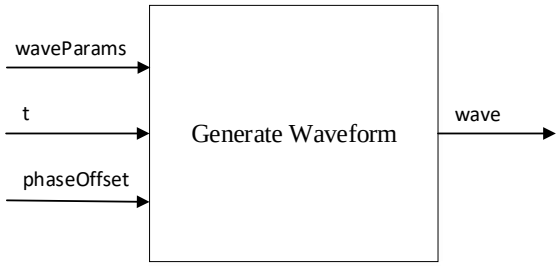

Figure 3.3: Input and output signals of waveform generation.

The respective input and outputs of the module are described below. The waveParams signal now incorporates an option to select a measured waveform.

- **waveParams**

  This is a structure which inherits several parameters. It determines which waveform should be generated and specifies the modulation frequency used by the system. Additionally other parameters which are required by the custom waveforms are included. It is possible to select individual measured signals which are then loaded from a .mat file.

- **t**

  In order to calculate the sensor response for specific discrete time steps this vector inherits the values which are required for this functionality. As a consequence its size depends on the simulation time-step set by the user.

- **phaseOffset**

  By setting this parameter unequal to zero a phase-shift of the signal which is generated can be achieved. This is important when creating the phase-shifted modulation signals for the different evaluation algorithms. Furthermore the distance dependent phase-shift can be considered.

- **wave**

  The final generated waveform is described by the output vector wave. It incorporates exactly one period of the requested waveform shifted by the specified phase-shift. The length of the output vector matches the corresponding input vector t.

3.3 Analysis of Systematic Errors

As described in section 2.2.1.1 two phase-images are sufficient for gathering a depth and amplitude map. Furthermore when maintaining low exposure-times the readout phase becomes the significant contribution to the overall power consumption as it is shown in table 3.1. By reducing the number of phase images the overall power profile can be drastically improved. However, due to the presence of systematic errors the results can be compromised. This section investigates the influence of these errors on a 2-phase evaluation. Therefore the DC errors of the incorporated 12 bit ADC's are examined. Its influence on the measurement is evaluated using a ToF simulator incorporating a model of the respective ADC. Furthermore the distribution of FPN across the sensor is examined. ToF measurements can be considered as evaluating complex phasors inside the unit circle. Hence the unit circle serves as an additional utility to investigate the impact of systematic errors.

3.3.1 ADC Transfer Characteristics

The incorporated ADCs are a source of errors. Each pixel is evaluated by them and the result is directly influenced by the introduced converter. These deviations can be categorized in AC and DC errors. The latter are of interest when investigating systematic deviations. Additionally quantization noise is introduced by the conversion process itself as it is described in section 2.3.2.5. The architecture of the integrated ADCs belongs to the family of nyquist-converters, because of the one-to-one relationship between input- and corresponding output-values. This classification is necessary, because the DC errors leading to systematic deviations are mainly valid for nyquist-converters [JM08].

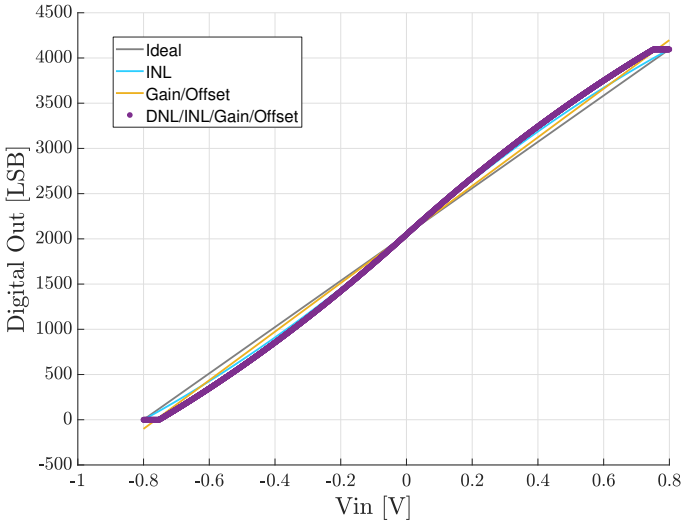

Figure 3.4: Transfer function of differential nyquist-rate ADC with increased INL.

Figure 3.4 shows the transfer-function of the used converters with increased INL value in order to see its effect. Due to the differential nature of the pixel's integration voltage the used ADC has to be additionally capable of evaluating negative voltages. Consequently, zero input-voltage of the function resides on the 2048 LSB output-word which is half of the resolution of a 12 bit ADC.

The positive and negative end of the transfer-function are saturated. This is due to the gain-error which alters the slope in order for this to happen. As a consequence the Full-scale range (FSR) is further reduced. An offset error additionally shifts the transfer-function along the y-axis.

Another DC deviation is the INL error. It is defined as the maximum divergence from the ideal linear transfer curve in LSB after subtracting gain and offset components. Subsequently the error function is a curve connecting the ends of the transfer-function and passes the point of maximum deviation from the ideal linear behavior. In a differential architecture this definition does not hold true. Instead the INL error has a different sign on the positive and negative input-range. The resulting error curve now incorporates both end-points, two-points of maximum deviation and zero. This is also visible in Figure 3.4.

Varying step-sizes of the ADC are described by the DNL error. An ideal converter employs step-sizes of exactly 1 LSB. A maximum DNL error of 0.5 LSB results in step sizes residing between 0.5 LSB and 1.5 LSB. If this error-source exceeds 1 LSB missing codes may be visible in the transfer-function. However, this does not have to be the case and depends on the specific distribution of the error. The DNL can be considered by using a gaussian function, because it is only describing a variation and is not fixed across the converter's input range [JM08].

Error	**Min**	**Typ**	**Max**	**Unit**
Gain error	-6.096	-4.713	-2.176	% FSR
DNL	1.594	1.906	2.438	LSB
INL	-2.392	-1.744	1.875	LSB
Offset Error	-13.94	-10.84	12.19	LSB

Table 3.2: Example specifications of the sensor ADC errors.

Table 3.2 shows example specifications for the above described error sources of the ADCs incorporated into the sensor. Offset and gain errors observable in the measurement are additionally determined by other factors like path length and column amplifiers. Due to this fact it is not sufficient to know the ADC parameters in order to mitigate them. Furthermore they are influenced by manufacturing mismatch and process variations which result in ADC devices yielding different error values.

3.3.2 Gain Error

Gain errors are constant factors amplifying each pixel read-out voltage. However, not every pixel yields the same gain value, because of the different ADC's and paths involved in the read-out. Each phase image is affected in the same way. The 0° phase-image represents the real whereas the 90° phase-image is a set of the corresponding imaginary parts of complex numbers. Equations shown in 3.3 highlight the impact of a gain error k on a captured pair of 0° and 90° phase-images.

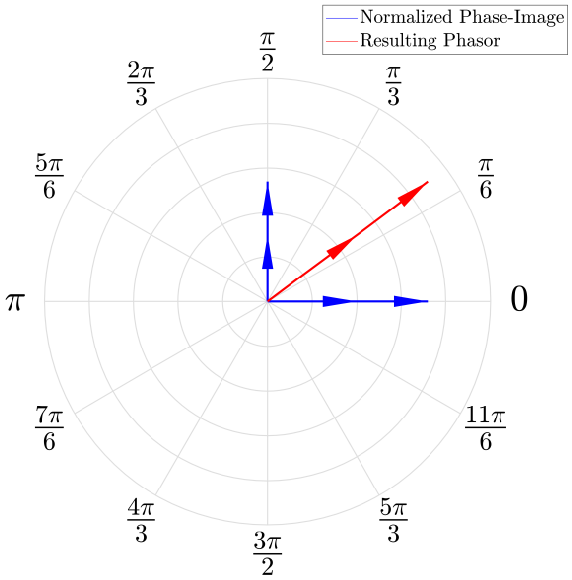

Figure 3.5: Representation of the gain-error utilizing complex phasors.

$$\begin{aligned} z &= a + ib \\ z_{gain} &= (ca) + i(cb) \\ \arg z_{gain} &= \arctan \frac{b\not{c}}{a\not{c}} \\ |z_{gain}| &= \sqrt{a^2c^2 + b^2c^2} \end{aligned} \tag{3.3}$$

Figure 3.5 shows that a constant factor multiplied to each phase-image does not change the result of the arctan calculation. Both complex phasors point in the same direction. Therefore a gain error does not influence the angle and subsequent distance calculation. However the magnitude changes, which results in deviations visible in the amplitude image.

3.3.3 Offset Error

Adding constant values to the various phase-images results in an offset error specific for each pixel. This error is mainly caused by a superposition of pixel manufacturing variations

and ADC offsets. It is described as FPN in section 2.3.1.3. By again utilizing the unit circle the effect of this error can be visualized easily. Figure 3.6 again shows a complex number, which is now altered by a constant value. This corresponds to a vector addition with a 45° phasor. As a consequence the magnitude as well as the corresponding phase angle is changed.

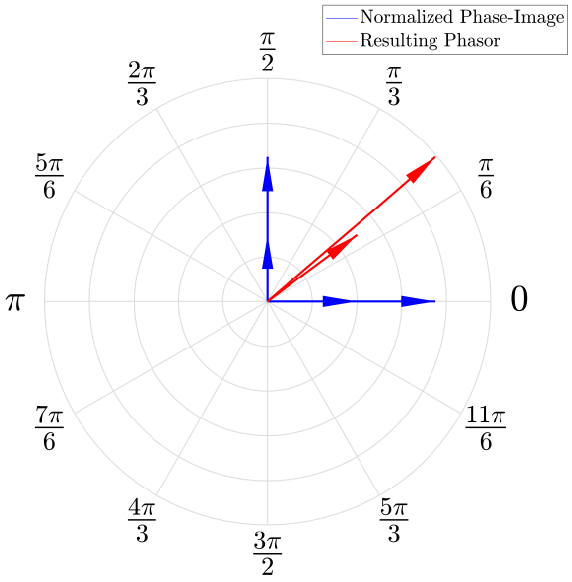

Figure 3.6: Representation of the offset-error utilizing complex phasors.

$$\begin{aligned} z &= a + ib \\ z_{offset} &= (a + c) + i(b + c) \\ \arg z_{offset} &= \arctan \frac{b + c}{a + c} \\ |z_{offset}| &= \sqrt{(a + c)^2 + (b + c)^2} \end{aligned} \tag{3.4}$$

As described by the equations found in section 3.4 this error has a negative effect on both depth- and amplitude-image. Depending on the error's magnitude the depth calculation yields a substantial deviation compared to the ground truth. Figure 3.7 shows the results of a simulation conducted with an offset error of 30 LSB which is a typical value found in current ToF sensor implementations.

It can be seen that this magnitude of error already leads to a phase which cannot be used for depth image creation. Therefore this error source needs to be compensated. However, in limited range the offset error leads to a smaller deviation when compared to larger distances. This happens due to an increasing loss in signal energy which is reflected back to the sensor. As a consequence the magnitude of the complex phasor is decreasing as well. Consequently the proportion between error- and signal phasor changes and alters the arctan calculation. Larger distances lead to a dominating constant 45° phasor which saturates the depth calculation. This is also visible in Figure 3.7.

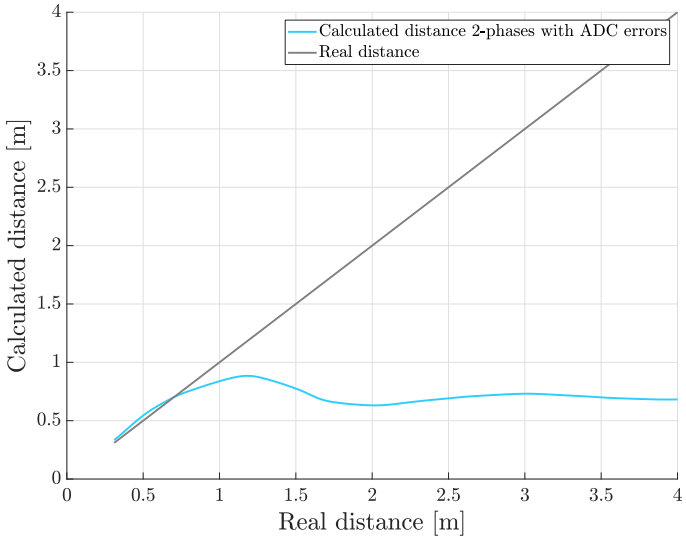

Figure 3.7: Effect of 30 LSB offset on the subsequent distance calculation using $t_{exp} = 0.5ms$.

3.3.4 Integral Non-Linearity Error

This non-linear distortion is introduced by the ADC's incorporated in the sensor. It is described in section 3.3.1 and is also visible in Figure 3.4. Utilizing the unit circle for error analysis is not conveniently possible, because this error source alters the complex phasor by introducing a non-linear distortion which depends on the respective pixel's read-out voltage.

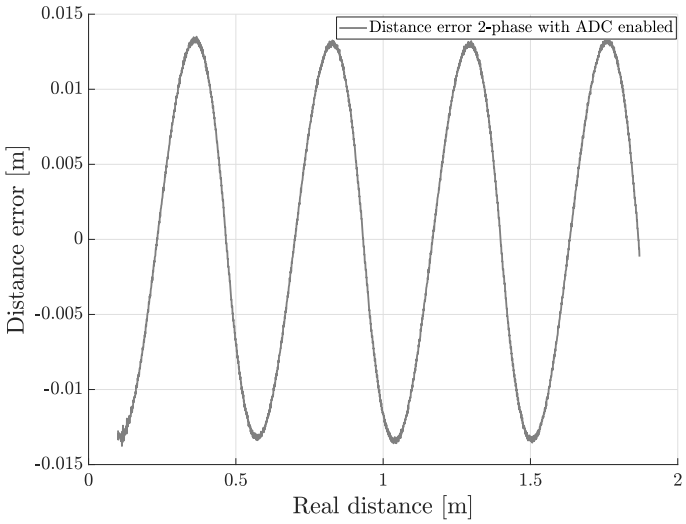

Figure 3.8: Effect of 200 LSB INL error on depth calculation.

To investigate this effect a simulation was conducted. All the other DC errors of the ADC model were set to zero in order to suppress their effects on the subsequent depth calculation. Additionally the modulation- and illumination-signal were set to be sinusoidal to avoid an overlapping between wiggling- and INL-error. The used simulation model includes the influence of distance change on the reflected power. Therefore the simulated sensor response yields a scaling which also complicates extracting the nature of the error. By setting a constant number of electrons collected by the pixel for each distance a constant sensor response function is achieved.

Inspection of the transfer characteristics shown in Figure 3.4 indicates that the highest deviation caused by the INL resides at approximately half of the positive and negative FSR. Now the read-out voltages were adjusted to reach this level. Figure 3.8 above shows the effect of -200 LSB INL error. It can be seen that it yields a similar behavior when compared to the wiggling-error. The curve shows its minima at $\varphi = 22.5°$ and its maxima at 67.5° in the first quadrant. Subsequent quadrants yield the respective highest deviation at mirrored versions of these angles. A minimum error is visible when φ is 0° or 45° and multiples of it. At 0° and other quadrant borders this happens due to one phase becoming infinitesimally small while the other has its highest value. The depth calculation therefore is not influenced by the offset introduced by the INL. This is because the relation $\frac{V_{90°}}{V_{0°}}$ still results in an infinitesimally small or large value. The small distance error at 45° can be explained due to both integration voltages being at the same value and both are consequently altered by the same offset. Conclusively this leads to the same result and an error value near 0.

Specifications of the ADC shown in Table 3.2 incorporate a significantly smaller value for the INL than used in the simulation. By utilizing the specified value of -1.744 LSB the resulting phase does not yield a deviation which introduces a relevant measurable error. As a consequence the INL can be considered to be of no importance in terms of contribution to the overall depth-error.

3.3.5 Differential Non-Linearity Error

DNL is also an effect caused by the non-ideal behavior of the incorporated ADC due to the deviation from an ideal 1 LSB stair-width. The description of this error can also be found in section 3.3.1. Its influence on the measurement was simulated by again utilizing the ADC model. All other systematic and temporal error sources were excluded. Illumination- and modulation-signal were again set to be sinusoidal and other ADC errors values were set to zero. Additionally the number of electrons collected in the pixel were kept constant during the distance sweep. The DNL error itself was modeled using a gaussian probability function with values residing in the range specified in Table 3.2. Those results were then added to the ideal step-sizes defined by the converter. Figure 3.9 shows the effect of the DNL on the simulation. It is visible that the distance deviation is well below 1 cm.

In practical implementations the values of the DNL do not employ a gaussian, but rather a different distribution. As a consequence the simulation results may significantly deviate

from the actual behavior. However, it can be considered as a worst-case analysis of the error source. In any case the DNL error cannot be compensated and is a fixed value introduced by the ADC implementation.

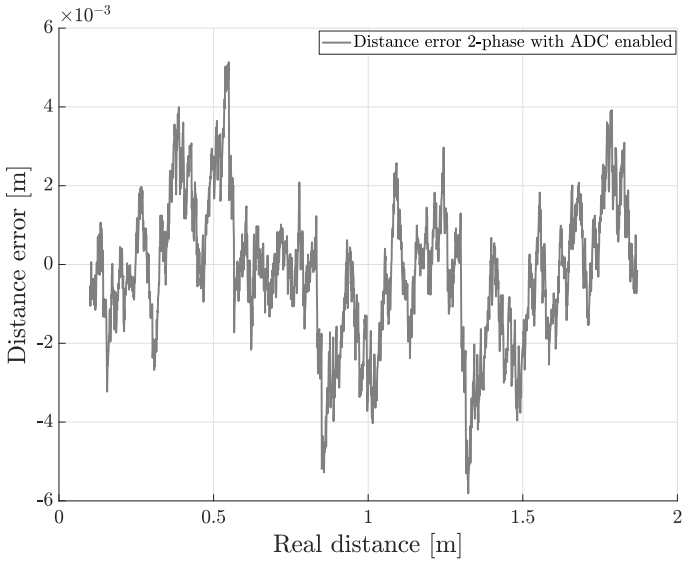

Figure 3.9: Effect of -1.744 LSB DNL error on depth calculation.

3.3.6 Wiggling Error

Another systematic error source which was further investigated is the wiggling error. Its origin is described in section 2.3.1.1. The influence of wiggling on the depth measurement is in theory the same when 2- and 4-phase evaluations are compared. Despite that asymmetries of the signal-path can introduce a significant difference in the wiggling-behavior of these evaluation algorithms. Simulations were conducted in order to quantify this effect. However, as the whole systematic deviations add up together in this error it is not possible to sufficiently analyze it without evaluating real-world data. The main problem of the 2- and 4-phase depth calculation algorithm lies in under-sampling the corresponding cross-correlation between illumination and modulation signal. Therefore it is not possible to recover the true shape of the resulting function. As a consequence the systematic deviation caused by the wiggling error can only be estimated in measuring the depth on several fine-grained discrete distances and comparing them to a ground truth. Typically a Linear Translation Stage (LTS) is utilized for this purpose, which places the image sensor on several distinct positions within sufficient resolution. This results in a significant time consumption as this has to be done for each hardware module separately.

In order to retrieve the real-world cross-correlation function the number of sampling points has to be increased. This is done by internally shifting the modulation signal in 15° instead of 90° steps. As a result the correlation function can be sampled at 24 points within one period. During the measurement the distance to a flat high-reflectivity surface was kept constant in order to avoid additional phase shift. However, the distance at which

the cross-correlation is sampled determines the initial phase offset of the function. In any case utilizing the above described method always results in exactly one full period which can be captured.

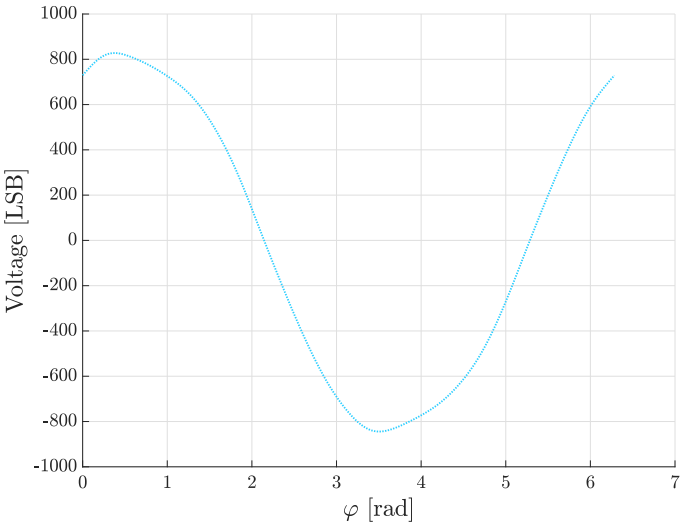

Figure 3.10: Captured and up-sampled cross-correlation function at the center pixel.

Figure 3.10 shows the gathered and up-sampled cross-correlation function measured on the center pixel of the array. The phase-images were further averaged in order to attenuate noise impact. It can be seen that the captured correlation function exhibits a sinusoidal-shaped waveform. Nevertheless there are higher-order fourier modes contained in the signal which lead to the mentioned depth deviation when utilizing it for the subsequent arctan calculation.

Extraction of the wiggling error was done by exploiting the fact that equation 3.5 leads to a linear slope connecting pi and $-pi$ respectively. However, it is required to use the arctan2 function in order to generate results for all four quadrants.

$$k(x) = \arctan2 \frac{cos(x)}{sin(x)} \tag{3.5}$$

By inspecting the equation above it can be seen that it represents the computation used for the depth calculation in an ideal environment by utilizing sinusoids. If these functions are now replaced by the captured cross-correlation the respective wiggling-error can be extracted. As mentioned earlier the measured function in Figure 3.10 is influenced by the distance in which the capturing was done. Therefore it is required to find the correct start index in which equation 3.5 results in pi. The functions $cos(x)$ and $sin(x)$ refer to the same captured cross-correlation function differing only in the indices used. As they are 90° phase-shifted and the function was sampled 24 times the resulting index offset is 6. Additionally the up-sampling factor has to be included as well.

Figure 3.11 shows the result of depth calculation utilizing both evaluation algorithms. The 4-phase calculation was established by using equation 2.3. 90° phase-shifts between the positions on the cross-correlation function were again achieved by adding the respective index offsets. It can be clearly seen that both evaluations are under the influence of the wiggling error due to the distortions present in the measured cross-correlation function.

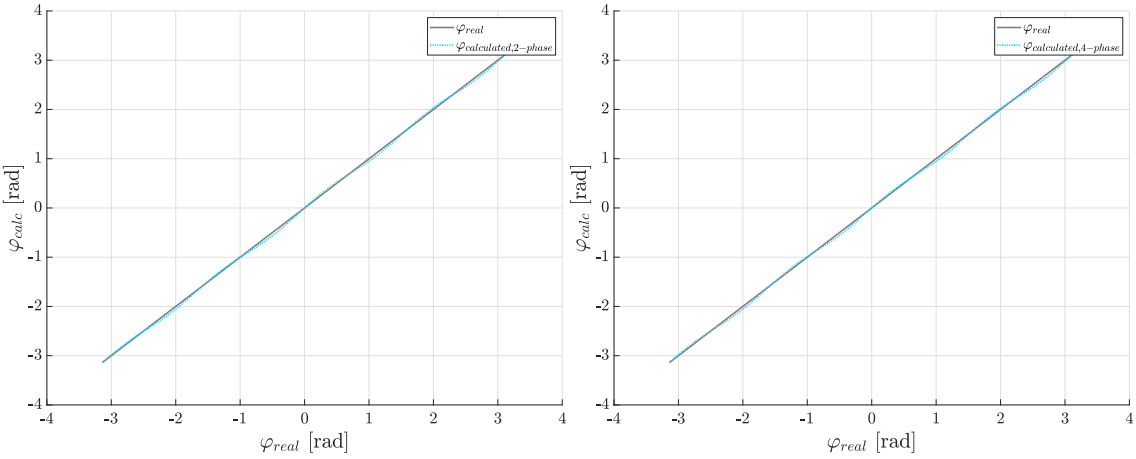

(a) 2-Phase depth calculation utilizing the measured cross-correlation function.

(b) 4-Phase depth calculation utilizing the measured cross-correlation function.

Figure 3.11: Depth calculation utilizing the measured cross-correlation function.

3.3.7 Countermeasures

The error sources described in section 3.3 do have different impact on the subsequent depth- and amplitude calculation. Generation of precise depth data does have higher importance and therefore the focus lies on the compensation of distance related errors. As further explained in the previous sections describing the systematic deviations, two main error components have to be compensated. Therefore it is necessary to compensate the offset error and additionally establish a wiggling calibration. The design of these processing steps is further explained in the subsequent sections. Furthermore the methods used for the compensation are illustrated and outlined.

3.3.7.1 FPN Compensation

As described in section 3.3.3 the offset error may introduce a significant deviation which needs to be compensated. The dark-frame in Figure 2.10 shows the FPN which sums up all offset errors. It clearly incorporates visual stripes which requires further investigations. Due to its repeating nature a statistical analysis is beneficial in order to detect regions of similar deviations. This could help in compensating this error source with less memory consumption. By inspecting the elements needed in order to digitize the pixel voltages a systematic approach in analyzing the offset contribution can be found.

The architecture of the read-out circuit is shown in Figure 3.12. For simplicity it only shows single-ended connections between pixels and surrounding circuitry as well as involved buffers. Conversion of the pixel's correlation voltages is done row-wise by enabling the corresponding row selectors. The sensor core incorporates 16 distinct ADC's and yields 432 columns. Consequently 14 ADC groups with each of them incorporating an even and an odd channel is formed. This enables them to simultaneously convert two pixel voltages in a ping-pong fashion. Every column of the pixel array is connected to a distinct source-follower which acts as an interface to the subsequent ADC channels. Connections between the converters and the columns follows a strict pattern. Therefore the first ADC's odd channel is converting column 0 and the corresponding even channel column 15 respectively. Column 31 does have the same read-out path as column 0 apart from the involved source-followers.

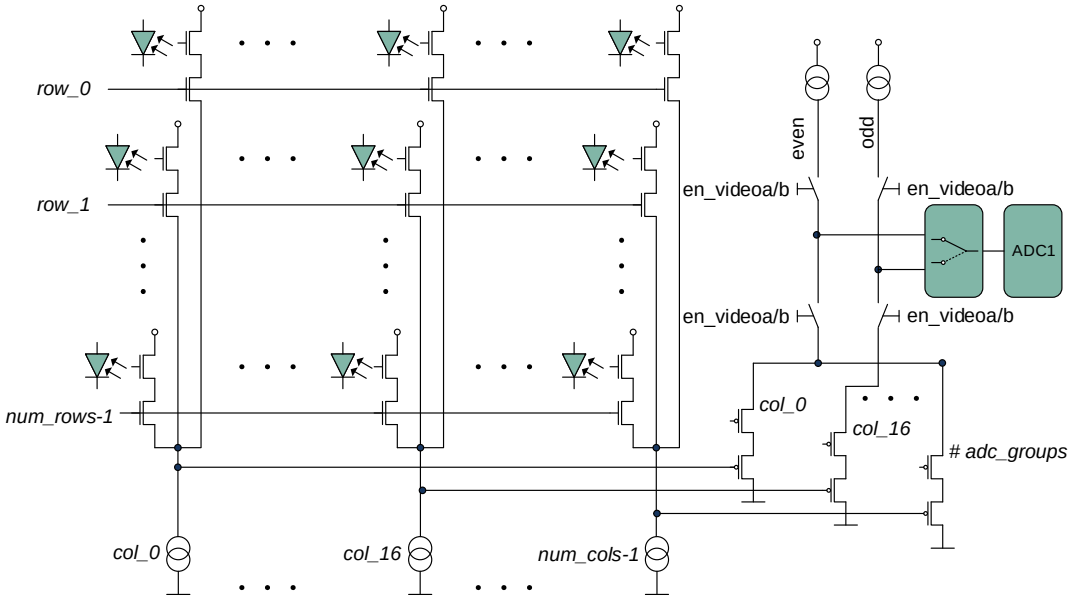

Figure 3.12: Read-out architecture of the pixel array.

Figure 3.13 depicts the overall FPN distribution across the image sensor. The mean value resides at approximately the ADC's mid-point corresponding to an offset of zero. However, the standard deviation yields almost 34 LSB. By again inspecting Figure 3.7 it can be seen that this amount of offset produces deviations which cannot be utilized by the subsequent depth calculation. Therefore it is not possible to estimate a global offset value which can be subtracted from every pixel.

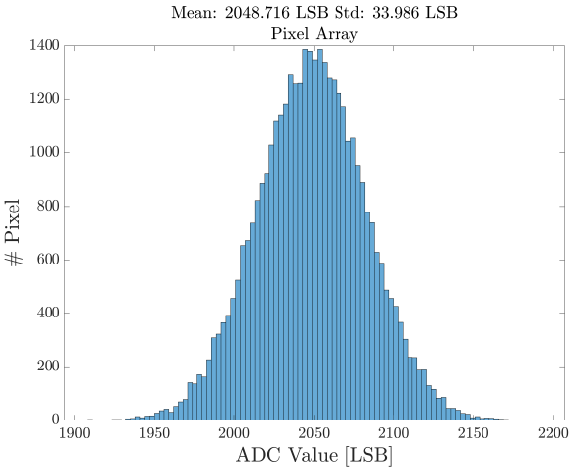

Figure 3.13: Distribution of FPN values across the pixel array.

Further analysis is necessary by examining pixel yielding similar components involved in the signal path. The visual stripes incorporated in the FPN image can be explained by the clustering of ADC's. As mentioned earlier each ADC converts the same columns in every row which results in the same offset contribution to the pixel's digitized integration voltages. In order to assess the similarity of pixels converted by the same ADC they were extracted. The distribution of this FPN values can be seen in Figure 3.14 below. It shows an example of pixels converted by the even and odd channels of ADC 8. The remaining converters were also analyzed and show similar values with respect to the standard deviation of the FPN. It can be seen that the offset contribution of the ADC's is not the main source of the error because the standard deviation still yields similar values when compared to Figure 3.13.

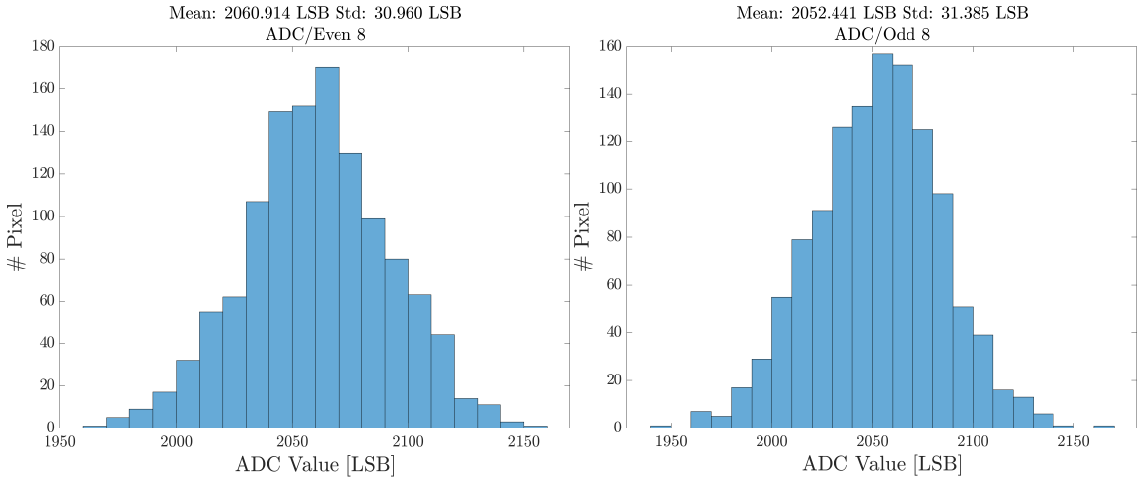

(a) Even channel (b) Odd channel

Figure 3.14: FPN of pixels converted by the same ADC channel.

As visible in Figure 3.12 all the pixels of the same column do have the same amplifier which is an additional source of error. By again investigating the FPN distribution of only these pixels it is possible to cancel out the influence of other column amplifiers and ADC's at the same time. When inspecting same rows on the image sensor a larger standard deviation is to be expected. This is due to the influence of all the different current sources and ADC's which are involved in the various signal paths connecting each row. Figure 3.15 shows the FPN distribution of row and column 100 as an example. It is clearly visible that pixels of the same column yield less standard deviation. On the other hand pixels in the same row have similar deviation from each other when compared to the overall array. Analysis of some distinct rows even showed standard deviations exceeding the value shown in Figure 3.13. Even though the analysis of FPN in the same columns shows better results it is also not possible to use a fixed offset for compensation purposes.

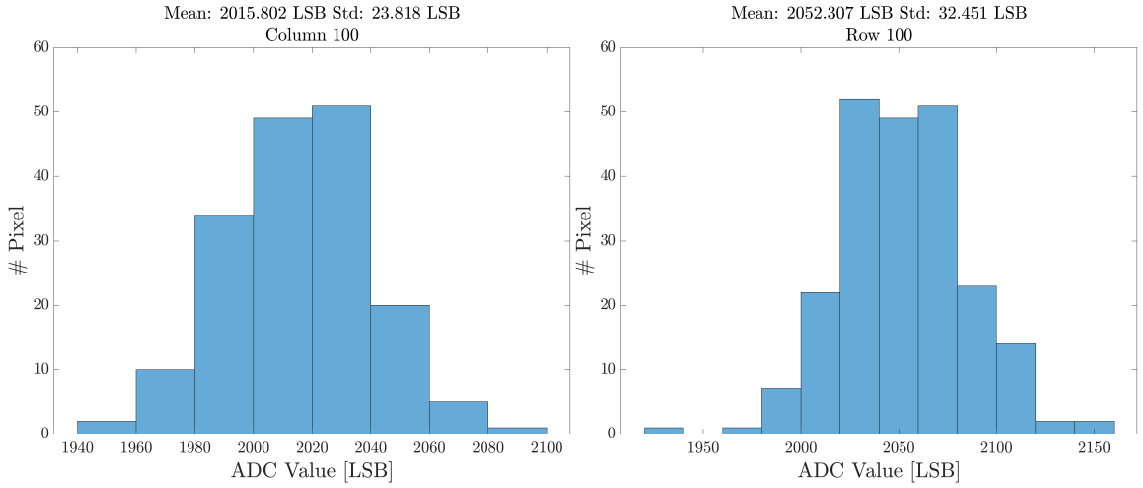

(a) Same column (b) Same row

Figure 3.15: FPN of pixels residing in the same column or row.

The pixel offset distribution shown above in Figure 3.15a does not show satisfying values. Another aspect which influences FPN are the electrical connections between pixels and the corresponding read-out circuit. They are internally routed from top to bottom of the sensor core. As a consequence the impedance increases between pixels while traversing down the same column. In order to asses the magnitude of this effect another analysis was done. By inspecting the distribution of the difference between subsequent FPN values of pixels beneath each other this can be established. Figure 3.16 below displays the variation of FPN delta for two distinct columns as an example. The standard deviation even exceeds the values measured across the whole pixel array. Additionally the delta values of different columns of the image sensor were investigated and show similar behavior.

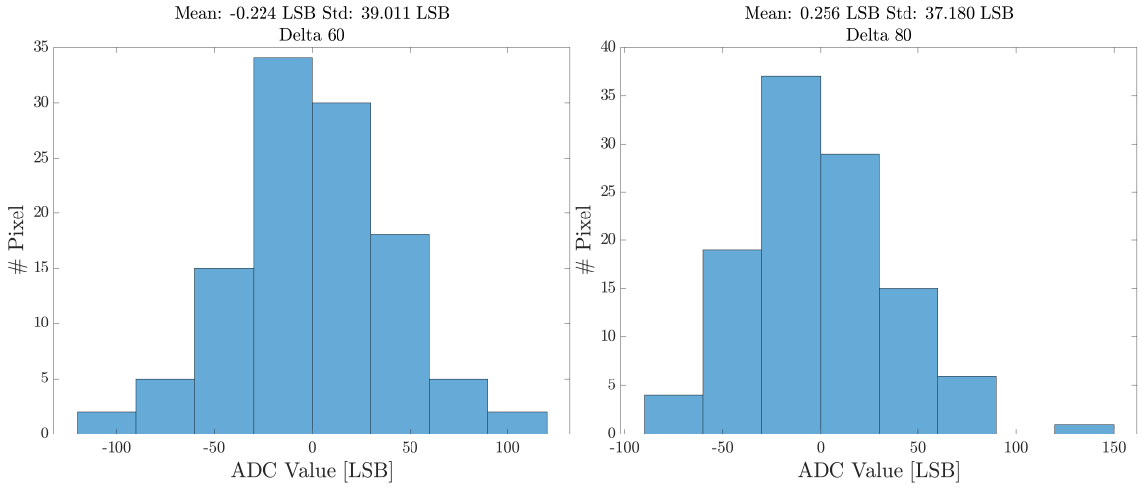

(a) Column 60 (b) Column 80

Figure 3.16: Distribution of FPN difference between pixels below each other.

The analysis described in this section shows that it is not possible to use a global value for the overall offset compensation. It is also not feasible to use a constant value for the same columns as well. Even vertically neighboring pixels do not show sufficient similarity as seen above in Figure 3.16. Another influence on the FPN is applied by the variations of the reset transistor which is depicted in Figure 2.6. As this effect is different for each PMD it cannot be systematically. Additionally there is a leakage effect which alters the reset voltage for each pixels. Conclusively the offset compensation can only be done accurately when saving each distinct offset value for every pixel.

3.3.7.2 Wiggling Correction

In section 2.3.1.1 the resulting depth calculation for 2- and 4-phase evaluations using the measured cross-correlation function were shown. Both clearly yield the impact of the systematic wiggling error. As a consequence both evaluation algorithms need a subsequent wiggling calibration. Compensation can be achieved by calculating the depth deviation from the ideal function $k(x)$ shown in equation 3.5. Now for each computed phase-shift the corresponding correction value is gathered from a LUT which inherits all compensation values. By increasing the size of the LUT the accuracy is further improved. However, this also results in a larger memory consumption. In order to still provide high accuracy with a reduced amount of compensation values, a polynomial fit can be used to interpolate between the distinct correction values.

By inspecting Figure 3.5 again it is visible that both evaluation algorithms lead to different wiggling behavior. Therefore their deviations from the ideal curve have to be saved for 2- and 4-phase evaluation separately. Figure 3.17 shows the extracted wiggling behavior for both algorithms on the center pixel.

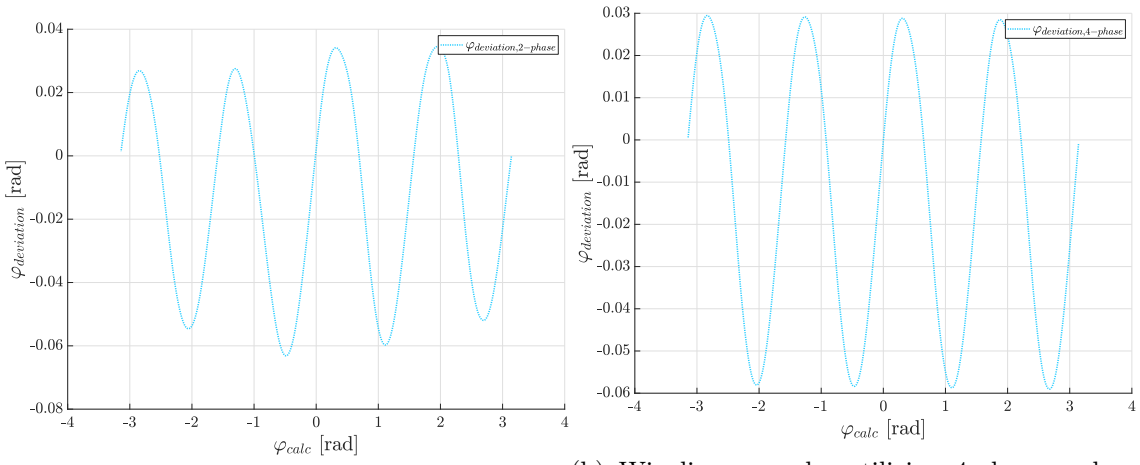

(a) Wiggling error by utilizing 2-phase evaluation.

(b) Wiggling error by utilizing 4-phase evaluation.

Figure 3.17: Extracted wiggling error for 2- and 4-phase evaluation algorithms.

Both shown above error functions yield the same magnitude of error. However, the 2-phase wiggling error incorporates varying amplitudes across the different phase values. As described in previous sections the 4-phase evaluation algorithm cancels out systematic errors. The error sources discussed in section 3.3 are mainly first order DC deviations. However, there are additional second order errors present which also influence the measurement. These are canceled out in the 4-phase evaluation, but are still influencing the 2-phase depth calculation. Furthermore the illumination power has shown to not be constant during the capturing of phase images. The VCSEL light-source is heating up during exposure and therefore the current is decreasing due to increasing internal resistance of the device. However, by using the corresponding LUT the error introduced by the non-linearities can be sufficiently canceled out.

3.4 Verification

In section 3.3 the systematic errors influencing the 2-phase ToF measurement were examined. They were mainly analyzed utilizing a simulation environment. Some error sources had to be measured directly in order to quantify their effect on the depth calculation. Therefore an evaluation framework was created in order to measure properties of the system and find a suitable low-power proximity sensing architecture. Additionally it was required to control a LTS to place the sensor system in an accurate absolute position with respect to a high-reflective white wall.

3.4.1 Setup

The existing measurement setup consists of a PC connected to a USB hub which establishes a gateway to communicate with both LTS and imaging system. Figure 3.18 shows the standard configuration used for measuring system parameters and evaluating the performance. The imaging module used for gathering ToF data is shown and explained in section 4.1.1.

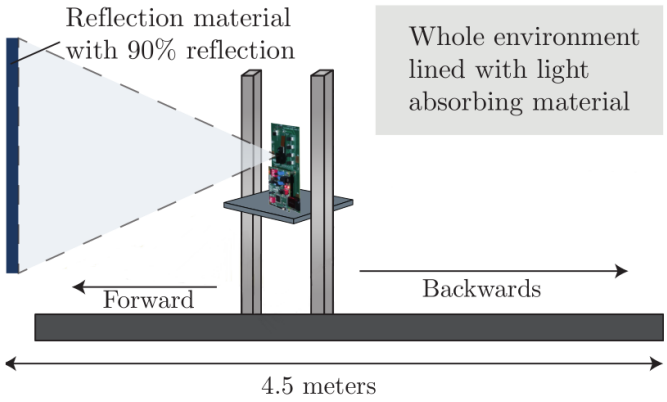

Figure 3.18: Measurement setup incorporating a LTS. Obtained with changes from [All18].

By utilizing the LTS stage it is possible to accurately position the sensor within only several centimeters up to 4.5 m. It allows step-sizes in the mm range and therefore offers high-resolution distance sweeps. The measurement target in most scenarios is a white-wall with a high-reflective surface of 90%. Background light is by default kept at a minimum to avoid systematic errors caused by it. The surroundings are covered in black color to absorb scattered light and as a consequence effectively reduce multi-path effects which could also alter the measurement. The vertical position of the sensor system itself can be additionally adjusted. This has to be done according to the FoV of the incorporated light-source and the maximum distance with respect to the white wall.

3.4.2 Evaluation Software

The software created for the verification process is split up in two parts. The first part is responsible for capturing and storing raw frames as well as controlling the LTS. Post-processing is done by a Matlab program which reads the captured frames and provides various options to analyze the phase-images and calculate the resulting depth- and amplitude values. Furthermore several functions are provided in order to visualize the captured data.

3.4.2.1 Image capturing

This part is responsible for raw-image capturing and controlling of the LTS. At the beginning the image sensor loads the corresponding configuration for the selected use-case. After this the driver which is responsible for the communication with the LTS is initialized and a connection is established. Subsequently the image sensor is positioned at the specified start location. The first phase-images are captured and stored as .mat files on the hard disk. If averaging is enabled the corresponding number of raw frames are gathered and the average is calculated using floating point precision. As a consequence for each distinct position there is a separate file present including the raw data in a structured way. This enables a comprehensive post-processing, because all the gathered data is directly available. In order to save disk space the resulting output folder can be compressed. Figure 3.19 shows a simplified activity diagram of the image-capturing software.

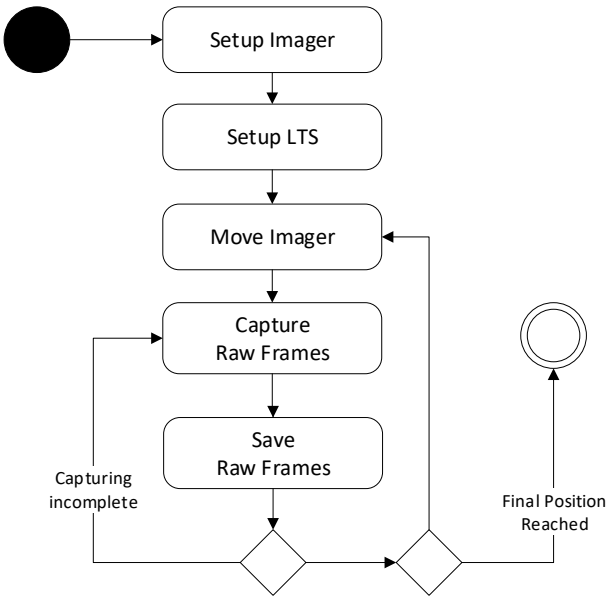

Figure 3.19: Simplified activity-diagram of the image-capturing software.

3.4.2.2 Post-processing

Post-processing of the captured raw-data is done by reading the files saved for each distinct position of the measurement. They are internally stored in a structure and provided to each developed function for further processing and analysis. Examining of the captured data in a flexible way by adjusting a provided Matlab script which specifies the various parameters. It is additionally possible to compare several distinct measurements by loading the raw-data from the corresponding folders and storing them in separate structures. Figure 3.20 shows the simplified activity-diagram for a basic depth- and amplitude calculation utilizing the described wiggling-calibration algorithm. Depth-calculation is done by either using the 2- or 4-phase algorithm. Additionally it is possible to select the quadrant of the respective 2-phase evaluation if at least 4 distinct phase images are available.

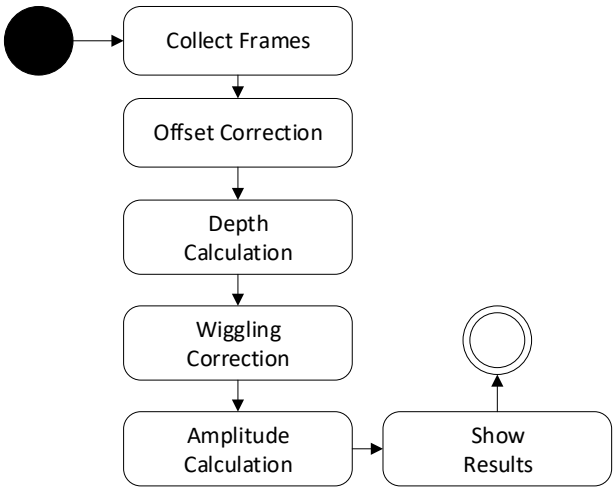

Figure 3.20: Simplified activity-diagram of the post-processing software.

Additional features are included in the post-processing software. It is possible to export calibration data for several systematic errors of the imaging system. Therefore functions are provided for FPN and wiggling calibration. Furthermore the proposed wiggling-calibration routine can be used to extract the corresponding LUT for depth-error compensation.

A rich set of analysis and plotting of measurement data is provided by functions. 3D surface plots of the scene can be created and exported. Statistical analysis of FPN distributions are established by specifying row- or columns as well as ADC channels. Furthermore the distance calculation can be visualized for distinct pixels and compared to the ground truth or another measurement. Hence the comparison between different evaluation algorithms and sensor configurations are easily possible.

3.5 Proximity Sensing Architecture

After exploration of the power-profile in section 3.1.2 and evaluation of the impact of systematic errors on the 2-phase depth measurement a suitable low-power architecture was found. Subsequent sections describe the hardware and software interactions as well as the measurement procedure itself. Implementation details of the proposed solution are outlined in section 4.4.

3.5.1 Hardware Structure

Figure 3.21 shows an overview of the physical connections between the essential parts of the imaging system. All the components are present on the hardware shown in Figure 4.1 which was also used for verification purposes. The illumination unit is directly controlled by the sensor which actuates a transistor connected to the VCSEL. Configuration of the sensor itself can be done by writing to special function registers using I2C. The cx-3 chip is responsible for receiving USB commands and subsequently write or read from the I2C interface. Furthermore it is capable of receiving raw data over two MIPI lanes and transfer them to the PC by again utilizing the USB connection.

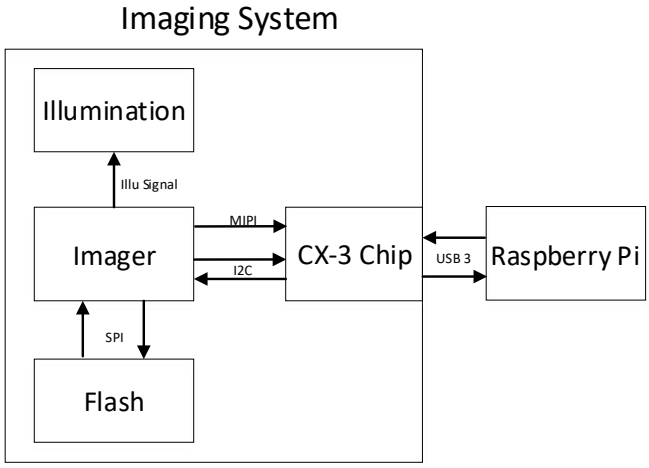

Figure 3.21: Overview of the system architecture.

In order to store calibration parameters and sensor configurations an external flash storage is present. Read and write operations are enabled by using a dedicated SPI bus. The sensor acts as a bridge between the PC and the flash storage. Data which is transferred to defined registers is then forwarded to the SPI bus. Furthermore the internal controller of the sensor is capable of reading its configuration from the flash upon sending a specified command over I2C.

3.5.2 Software Structure

The designed software architecture for proximity sensing is represented in Figure 3.22 by means of a class diagram. It shows the connections between the distinct modules responsible for each required part of the processing. Furthermore it highlights the most important members and methods of the respective classes. The architecture is split up between user-interface and functionality. Starting of measurements is initiated by the user. After new depth data has arrived the resulting depth frame is shown on the screen. Error corrections, algorithms and exposure times can be also specified using the GUI.

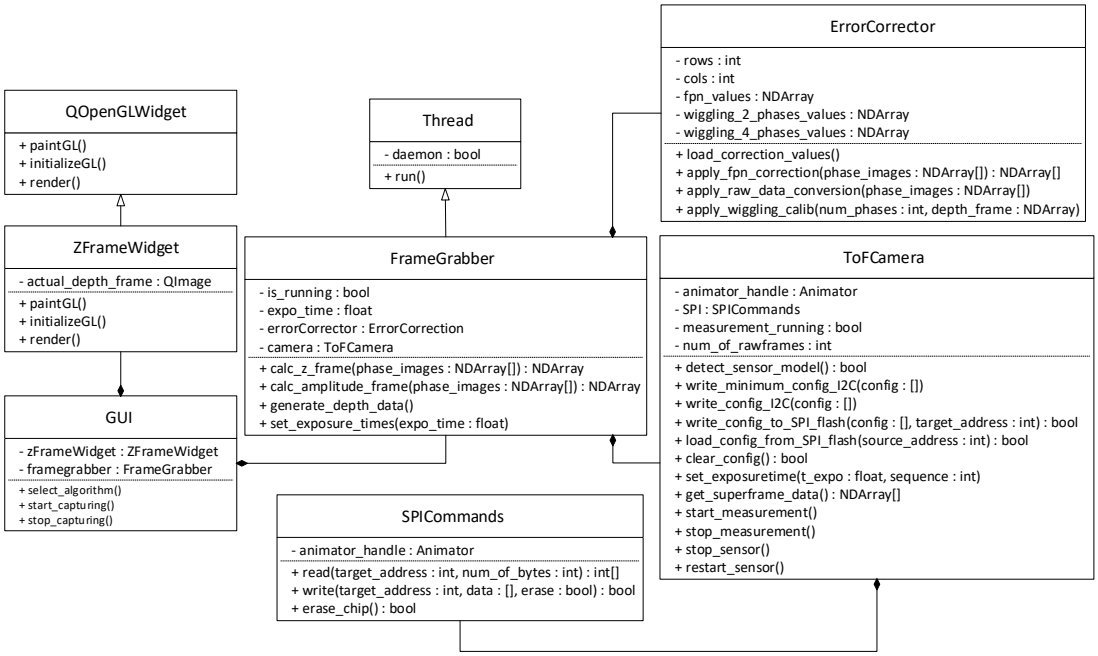

Figure 3.22: Class diagram of the proximity sensing architecture.

All important functional components are inherited by the **FrameGrabber**. It is derived from the Thread class and operates as a daemon which repeatly executes the low-power measurement. Raw-data collection and error compensation is done by utilizing the respective methods provided by the responsible classes. Furthermore the depth calculation is executed and a colormap is applied. Upon finishing of the depth-image creation the GUI is informed to update its content.

The **ErrorCorrector** class is responsible to load and apply the respective offset and wiggling compensation values which are needed for an accurate 2-phase evaluation. They are imported from data captured by the error extractions which are described in sections 2.3.1.3 and 3.3.7.1 respectively.

An abstraction of the imaging system is achieved by the **ToFCamera** class. It incorporates functionality to configure the sensor and gather raw data which can be subsequently used for depth calculation. Furthermore low-level GPIO signals can be set and reset. This enables to completely shut-down the image sensor. In order to ease SPI communication a **SPICommands** helper class is incorporated. The class additionally incorporates an animator member for low-level communication with the cx-3 controller. It is an instance of a C++ wrapper as it is described in section 4.1.3.

3.5.3 Dynamic Design

Proximity sensing does not require high refresh rates and large ranges which have to be covered. Therefore the selected use-case yields 1 FPS and exposure-times below 0.5ms. By inspecting table 3.1 it is visible that the energy during the idle state marks the main contribution to the overall power consumption when operating the sensor at low FPS. Furthermore the energy required for readout of pixel data is larger compared to the capturing phase when utilizing small exposure times. Therefore the 2-phase evaluation algorithm was selected for depth calculation.

Figure 3.23 shows a simplified activity diagram of the proposed sensing architecture. As mentioned earlier in section 3.5.2 controlling of the sensor, gathering of raw data and depth calculation is done on a separate thread. Starting and stopping of the measurement itself is established by the user utilizing a GUI.

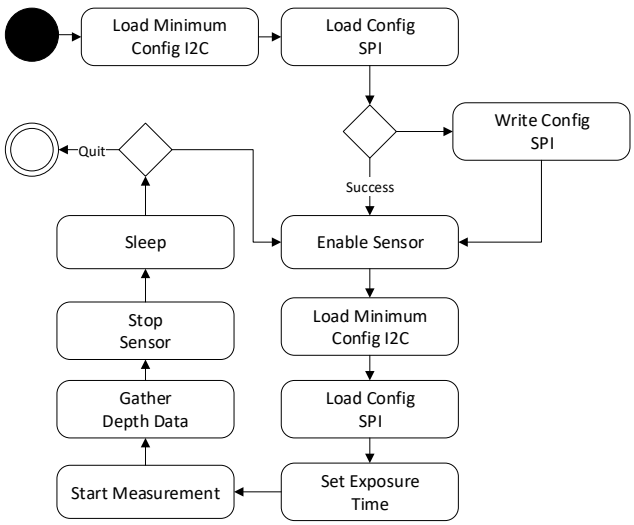

Figure 3.23: Simplified activity diagram of the proximity sensing architecture.

Upon creation of the **FrameGrabber** a minimal configuration is written to the image sensor over I2C. This is required for start-up as it determines system parameters for the internal blocks. After that the full sensor configuration is loaded from the SPI flash. If this operation fails there are no valid parameters residing on the external memory. Therefore

the whole configuration is subsequently written to it. After these steps the measurement loop is entered which is repeated until external termination by the user.

Exposure times have to be re-set in every loop iteration, because it is overwritten by the fixed values defined in the external SPI flash. The measurement is started and raw data is collected until all phase-images of the use-case are gathered. Additional offset and wiggling corrections are applied, the color-mapped image data is extracted and a refresh of the GUI is scheduled. Upon finishing this operation the image sensor is stopped by writing to the respective registers and subsequently setting the reset pin to a low-state. After that the thread sleeps for a specified amount of time. This approach drastically lowers the idle-time and therefore the overall power-consumption.

Chapter 4

Implementation

This chapter incorporates the description of the established software. It covers the implementation of extensions for an existing ToF simulator and an evaluation software. Furthermore the used hardware and software environment is illustrated. Additionally the implementation of the proposed low-power measurement is explained.

4.1 Development Environment

The subsequent sections describe the software and hardware platforms used for the implementation environment. It gives a short explanation of the usage and applications of them.

4.1.1 Hardware platform

In order to validate and establish the proposed measurement approach an imaging platform was selected. Figure 4.1 shows the used system. It incorporates every element which is needed for measurement and communication purposes. For transferring data between the system and external PC's a cx-3 chip is present.

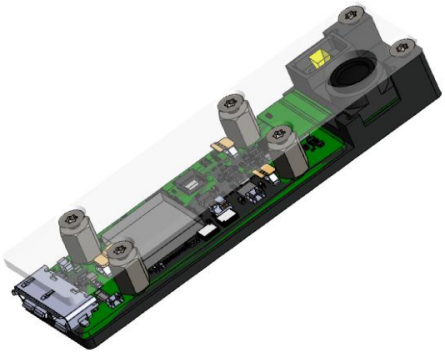

Figure 4.1: ToF imaging platform incorporating the IRS1645 sensor. Additionally a cx-3 communication chip and a VCSEL is present on the PCB.

It reads out the raw-frames of the image sensor using the MIPI standard and transfers it using an USB connection. Additionally commands for sensor configuration can be received

and are subsequently transferred to the imager by utilizing a SPI channel. The system is covered with a housing and a micro-lens is mounted in front of the image sensor. Its VCSEL light-source is located next to the pixel array and yields an output power of 1 W.

4.1.2 Matlab

Matlab is a programming language dedicated for solving mathematical problems and is based on using matrices for calculations. Due to this nature it is convenient for simulation purpose and processing of raw-frames coming from the imaging system. It was used for the implementation of the ToF simulator extensions and the evaluation software. Plotting and exporting of simulation and measurement results is easily possible using various build-in functions. Furthermore image data can be imported by parsing the corresponding .mat files exported by the python measurement program. Each of the proposed programs were written using Matlab 2018b.

4.1.3 Python

In order to retrieve raw frames from the camera, a python wrapper utilizing C++ functions is available. It uses the Royale SDK which was created by PMD technologies. The PyCharm 2018.3.5 Intregrated development environment (IDE) was used to create a logging software which actuates the LTS and retrieves image data for every distinct position with respect to a white wall. The implemented logging software itself hereby uses the above mentioned python wrapper to communicate and retrieve raw frames. For each position the corresponding data is saved in a .mat file which can be further processed. Furthermore the proposed measurement procedure was implemented using Python. Additionally the QT5 framework was used for the design of an user-interface. It provides a convenient way for the creation of platform independent GUIs.

4.2 Simulation Model

The used ToF simulator which is extensively described in [All18] had to be extended by a new ADC model. Additionally the possibility to incorporate the actual waveform of the illumination signal was implemented. The model itself is developed using Matlab and therefore the extensions were also implemented using this programming languag by modifying the corresponding modules. In the subsequent sections the specific implementation details regarding the described extensions are explained.

4.2.1 ADC

The ADC model was implemented by means of a Matlab function. Respective inputs are passed as parameters. A struct holding the ADC properties is read-out and the model

is adjusted accordingly. The respective transfer behavior is calculated in several steps integrating the DC errors. Figure 4.2 shows the resulting function as a superposition of the various deviations. It is scaled in order to visualize the discrete steps within the transfer curve. The dots represent the center of each respective step in the output. If no offset error is present the transfer curve intersects zero input voltage yielding the mid-point value of 2048 LSB.

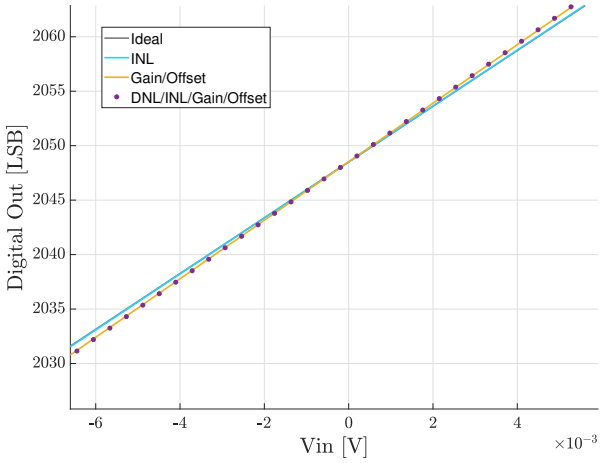

Figure 4.2: Discrete ADC transfer characteristics.

The final output words are derived by utilizing a table lookup. Listing 4.1 shows this procedure by using a build-in Matlab function. The corresponding output value is the nearest neighbor with respect to the input voltage. This behavior matches the real conversion process established by the ADC. Finally the converted digital value is further processed to provide a signed result. This is necessary for the subsequent depth calculation.

```
raw = interp1(x_final, TFlimited, voltage, 'nearest');

modeled.raw = ((raw − d_ideal) / d_ideal) .* Vref;
```

Listing 4.1: Table lookup used to implement the conversion process.

4.2.2 Illumination Waveform

As described in section 3.2.2 the existing waveform generation was extended. Therefore the possibility to import a measured illumination signal was implemented within the ToF simulator. The generate_waveform function evaluates the respective input parameters and reads out the waveParams structure. Within this variable there is a flag present which selects the respective waveform which should be generated by the function. Listing 4.2

shows the import of measurement data into the simulation. Furthermore an interpolation is done in order to match up the vector size used internally by the simulator to calculate the sensor response function.

```
illuWaveMeasured = load('illu_waveforms/illu_waveform.mat');

illuWaveMeasured = illuWaveMeasured.illuWaveMeasured;

illuWaveInterpolated = interp(illuWaveMeasured, ...
        floor(5000 / length(illuWaveMeasured)))';
```

Listing 4.2: Loading and interpolation of the measured waveform.

Figure 4.3 shows the measured illumination waveform utilizing an optical probe and an oscilloscope. The y-axis corresponds to the output of the optical probe and is further scaled to yield a maximum amplitude of 1. This is necessary, because the output power of the illumination light-source is already considered within the simulation model. It can be seen that the measured waveform does not show a rectangular shape but is influenced by the effects of the VCSEL. This is mainly caused due to input capacitance and self-heating. As a consequence the simulator is able to provide more accurate results with respect to real-world data. However, it is necessary to import the correct measurement data for each distinct light-source configuration and modulation frequency.

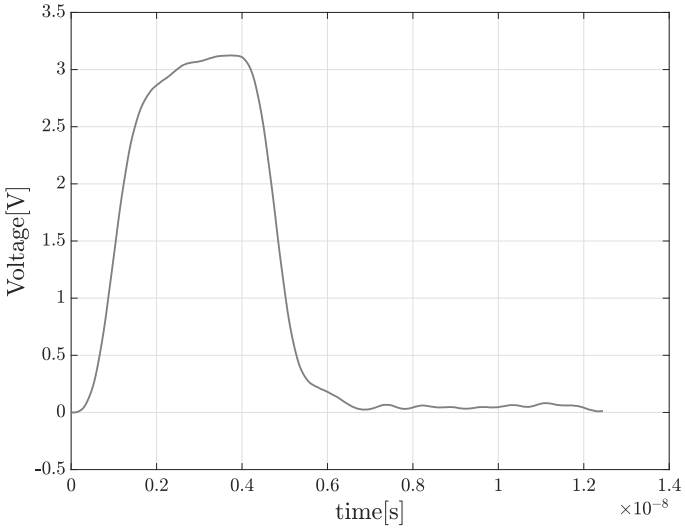

Figure 4.3: Measured illumination waveform utilizing an optical probe connected to an oscilloscope.

4.3 Evaluation Software

The following sections describe the implementation of the software used for gathering and evaluation of real-world ToF data. Furthermore the error corrections such as FPN compensation and wiggling calibration techniques are outlined. The most important functions are highlighted and the used data-structures are explained.

4.3.1 Image capturing

Gathering of raw data and setup of the imager was done by utilizing the Animator API written in Python. Furthermore the control of the LTS was established by a helper class providing functions for accurate positioning within the specified range outlined in section 3.4.1.

4.3.2 Error extraction

Sections 4.3.2.1 and 4.3.2.2 describe the implementation of the error extraction in order to utilize the gathered data to improve the subsequent depth calculation. The most important code fragments are condensed and explained. Furthermore the additional implementation details are outlined.

4.3.2.1 Extraction of FPN

In order to gather the FPN described in section 2.3.1.3 it is necessary to capture a dark-frame within minimal exposure-time. As a consequence the corresponding use-case is deployed on the sensor and data is gathered using the Python image capturing described in section 4.3.1. Subsequently the data is read from the respective files and loaded into a structure. The first phase-image yields the dark-frame and is saved into a .mat file. The following procedure has to done for each sensor individually as they yield different FPN values.

```
function [] = fpnCalib(measurement)

fpnOffset = measurement.position{1, 1}.frames{1, 1}.phase_img_0;

% save fpn offset
save('fpn_calib.mat', 'fpnOffset');
end
```

Listing 4.3: Storing of FPN values.

4.3.2.2 Acquiring of wiggling deviations

The wiggling calculation is established by utilizing a use-case with 24 phase-images each yielding a phase-shift of 15° in order to sample the overall resulting cross-correlation function. The method is extensively described in section 3.3.6. Listing 4.4 shows its implementation for the 2-phase depth calculation algorithm. The AKFi vector incorporates the up-sampled cross-correlation measured throughout a constant distance with respect to the high-reflective white wall. Furthermore the captured phase-images were averaged in order to mitigate the errors introduced by noise components which are explained in section 2.3.2.

```
indexPhase0=AKFPosPi;
indexPhase90=indexPhase0+indexShift90;

for count = 1 : N
 indexPhase0 = indexPhase0 + 1;
 indexPhase90 = indexPhase90 + 1;

 if indexPhase90 > N
  indexPhase90 = 1;
 end

 if indexPhase0 > N
  indexPhase0 = 1;
 end

 calcPhi2(count) = atan2(AKFi(indexPhase90), AKFi(indexPhase0));
end
```

Listing 4.4: 2-phase depth calculation for wiggling calibration.

AKFPosPi is the start-index for the arctan2 calculation which subsequently yields π as a result. This is necessary when comparing the results with the linear function connecting π and $-\pi$ respectively. Depending on the distance between sensor and wall, a phase-shift in the sampled cross-correlation can be observed. Therefore the start-index has to be re-calculated if the measurement setup changes.

The same procedure is utilized when evaluating the wiggling error for the 4-phase algorithm. However, it is necessary to add two additional variables holding the respective values for a phase-shift of 180° and 270°. Depth calculation is done by evaluating equation 2.3 respectively. The sampled cross-correlation serves as input for the respective parameters and indices are calculated following the method shown in Listing 4.4.

Listing 4.5 shows the calculation and exporting of the wiggling calibration values for the 2-phase algorithm. For each distinct phase the deviation with respect to the ideal curve is derived and stored in diffPhi2. Subsequently this vector is exported into a .mat file which can be used to correct the calculated depth-image. The same is done for the 4-phase evaluation utilizing the corresponding deviation values.

```
phiVector = linspace(pi , -pi, N);

diffPhi2  = (calcPhi2 - phiVector);

save('wiggling_calib_2_phases.mat', 'diffPhi2');
```

Listing 4.5: Calculation and export of wiggling-calibration values.

4.3.3 Post-processing

Subsequent sections describe the implemented post-processing after importing the measured raw sensor data into the Matlab environment. By applying these methods the resulting depth image yields improved results regarding overall measurement accuracy. The compensation values which were acquired by utilizing the implemented error extraction described in section 4.3.2 are exploited for correction purposes.

4.3.3.1 Offset correction

After read-out of the raw data and storing them in the corresponding structures the subsequent depth- and amplitude-calculation can be established. However, when utilizing a 2-phase evaluation the offset error influences the result drastically as it is described in previous sections. Therefore the gathered phase-images are corrected using the offset matrix which holds the FPN values.

```
fpnOffset = load('fpn_calib.mat');

offsetMatrix = fpnOffset.fpnOffset;

phase_img_1 = phase_img_1 - offsetMatrix;
phase_img_2 = phase_img_2 - offsetMatrix;
phase_img_3 = phase_img_3 - offsetMatrix;
phase_img_4 = phase_img_4 - offsetMatrix;
```

Listing 4.6: Offset compensation of the captured phase images for a mode-5 use-case.

Additionally a signed output is established and conversion of the ADC results is not necessary anymore. Listing 4.6 shows the compensation of a mode-5 use-case. The procedure is the same for each use-case. Every incorporated phase-image has to be compensated using the same offset matrix.

4.3.3.2 Depth and amplitude calculation

For each set of phase-images the corresponding depth- and amplitude images are derived. The calculations follow the definitions given in section 2.2.1.1. Listing 4.7 shows the depth calculation utilizing the offset corrected phase-images. This is done in a loop for each discrete distance step in the measurement. Furthermore there is the possibility to capture several superframes within each position on the LTS. This is also considered in the calculations shown below. The built-in arctan2 function is used to generate results for all four quadrants. This is achieved by looking at the respective sign of the input values. Additionally the output has to be corrected in order to provide results in the interval $[0, 2\pi]$ instead of $[-\pi, \pi]$.

```
phase_img_1 = measurement.position{1, stepCounter}.frames{1, framePos}.phase_img_1;
phase_img_2 = measurement.position{1, stepCounter}.frames{1, framePos}.phase_img_2;
phase_img_3 = measurement.position{1, stepCounter}.frames{1, framePos}.phase_img_3;
phase_img_4 = measurement.position{1, stepCounter}.frames{1, framePos}.phase_img_4;

calcDepth = atan2(phase_img_2 - phase_img_4, phase_img_1 - phase_img_3);
```

Listing 4.7: 4-phase depth calculation utilizing the captured phase-images.

Listing 4.8 shows the amplitude calculation inside the corresponding implemented Matlab function. It uses the raw-data of a mode-5 use-case operating with four distinct phase-images. The function call also takes place after offset correcting the input data.

```
phase_img_1 = measurement.position{1, stepCounter}.frames{1, framePos}.phase_img_1;
phase_img_2 = measurement.position{1, stepCounter}.frames{1, framePos}.phase_img_2;
phase_img_3 = measurement.position{1, stepCounter}.frames{1, framePos}.phase_img_3;
phase_img_4 = measurement.position{1, stepCounter}.frames{1, framePos}.phase_img_4;

calcAmplitude = sqrt(phase_img_4 - phase_img_2).^2 + ...
(phase_img_1 - phase_img_3).^2) / 2;
```

Listing 4.8: 4-phase amplitude calculation utilizing the captured phase-images.

4.3.3.3 Wiggling Correction

After deriving the depth images of the measurement, a wiggling correction is applied. The corrections utilize the data generated by the implementation of the wiggling extraction shown in section 4.3.2.2. Data is loaded from a .mat file and a table lookup is used to gather correction values for each calculated phase value. This is achieved by using the build-in function **interp1()** with the nearest neighbor interpolation algorithm. Subsequently the correction values are subtracted from the derived depth value. Before utilizing the proposed correction it is necessary to compensate the FPPN component influencing the depth calculation. However, as the center-pixel was used for evaluation purposes this step was skipped even though the functionality was implemented.

```
diffPhi2 = load('wiggling_calib_2_phases.mat');

phiDiffWiggling = interp1(interpAxis, diffPhi2.diffPhi2, calcDepth, 'nearest');

calcDepth = - (calcDepth - phiDiffWiggling);
```

Listing 4.9: Wiggling calibration applied to the respective input data.

4.4 Implementation of the Proximity Sensing Architecture

The proposed proximity sensing architecture described in section 3.5 was implemented using the Python language and the QT5 framework. Therefore it is independent of the operating system and can run on a resource-constrained device such as a Raspberry Pi. All of the error corrections provided by this implementation were ported from Matlab to Python. They correspond to the descriptions given in section 4.3.3. As a consequence only the Framegrabber implementation is explained in this section, because it covers the most important part of the established software.

```
def setup(self):
  self.camera.load_minimum_config_I2C(self.camera.mode.full_cfg)

  if self.camera.load_config_from_SPI_flash(self.camera.spi_target_address) is False:
      self.camera.write_config_to_SPI_flash(self.camera.mode.full_cfg,
                                            self.camera.spi_target_address)
```

Listing 4.10: Setup of the Framegrabber.

Listing 4.10 shows the setup of the camera hardware which is called in the constructor of the Framegrabber. A minimum configuration is loaded into the respective special function registers for sensor start-up. If the full register settings cannot be gathered from the SPI flash they are subsequently written to it.

```
def run(self):
  while self.is_running:

    self.camera.restart_sensor()
    self.camera.load_minimum_config_I2C(self.camera.mode.full_cfg)
    self.camera.load_config_from_SPI_flash(self.camera.spi_target_address)
    self.set_exposure_times(self.expo_time)
    self.camera.start_measurement()

    self._generate_depth_data()

    self.camera.stop_measurement()
    self.camera.stop_sensor()

    time.sleep(self.sleep_duration)
```

Listing 4.11: Core functionality of the Framegrabber.

The Python implementation shown in Listing 4.11 represents the measurement loop displayed in Figure 3.23. Access to the camera is made by utilizing an instance of the **ToF-Camera** class. The sensor is repeatably shut-down completely and only actively operated in a small time window. Due to the hard reset, the sensor configuration has to be loaded each time before starting a measurement. In order to provide flexible exposure-times it is additionally required to overwrite the respective special function registers. This is done by accessing the I2C bus which connects the cx-3 chip and the image sensor as it is shown in Figure 3.21.

Inside the generate_depth_data() method several processing steps are established. The raw data of a single superframe which incorporates all phase-images is captured. This is a blocking procedure and subsequent calculations are performed upon receiving all of them. Afterwards the resulting phase-shift of the pixels are computed by exploiting numpy arrays. If offset compensation is enabled the FPN values are subtracted from each phase-image individually. Otherwise the fixed ADC mid-point value is used to provide signed LSB values for the arctan2 calculations. Furthermore wiggling-calibration is applied if it is enabled by the user. The implementation is similar to the Listing 4.9 shown in section 4.3.3.3. Conclusively the calculated and colormapped depth image is converted to a format which can be processed by the Qt framework. By calling the update() method of the **ZFrameWidget** class a refresh of the GUI window is issued.

Chapter 5

Results

The following sections in this chapter deal with the comparison between the established standard for depth calculation and the proposed procedure. Therefore real-world measurements and simulations are compared in order to show the performance of the new approach. Furthermore the power-profile of the proximity sensing architecture outlined in section 3.5 is investigated and compared to those of different sensors from other manufacturers shown in section 2.4.2.

5.1 Comparison between 2- and 4-phase depth calculation

This section investigates measurement and simulation results concerning 2- and 4-phase depth calculation. Extensive analysis of the impact of systematic errors on depth calculation were conducted in section 3.3. However, all influences can only be incorporated if measurements are performed. This is necessary to quantify the deviations between the two evaluation algorithms both with and without implemented error corrections.

5.1.1 Preconditions

If not otherwise stated the measurements were conducted within the environment described in Figure 3.18. Consequently the following conditions apply

- Throughout the measurements minimal background light was present in order to mitigate its influence on the measurement.
- The target was a high-reflective uniform white-wall to provide a good SNR.
- The captured raw phase-images were averaged sixteen times. This was done to reduce the impact of the various noise sources outline in section 2.3.2.
- FPN was compensated beforehand. As it is described in section 3.3.3 this error source has to be eliminated in order to provide usable depth information with the 2-phase evaluation.
- Phase-jumps caused by the limited unambiguity range are unwrapped. During the distance sweep they occur at about 1.8m due to the internal operation frequency of 80MHz.

- The center pixel was used for depth calculation. This is due to avoid the influences of the involved micro-lens which has to be further calibrated.
- For the 2-phase evaluation the exposure time was set to be twice as long when compared to a 4-phase measurement. This is due to the Equation 2.3. When utilizing the symmetry of the integration voltages and evaluate the before mentioned expression the result shown in Equation 5.1 is obtained. Therefore a better SNR is achieved in contrast to a single 2-phase measurement when operating with the same exposure times.

$$\begin{aligned} u_{pmd,0^\circ} &= -u_{pmd,180^\circ} \\ u_{pmd,90^\circ} &= -u_{pmd,270^\circ} \\ \Rightarrow \varphi_{ToF,4-phase} &= \arctan \frac{2 \cdot u_{pmd,90^\circ}}{2 \cdot u_{pmd,0^\circ}} \end{aligned} \tag{5.1}$$

5.1.2 Distance sweeps

By utilizing the setup shown in section 3.4.1 distance sweeps yielding a step-size of 0.5 cm were conducted. The results of both algorithms are presented in the following sections. Furthermore they are compared against each other regarding their accuracy and deviation with respect to the ground truth.

5.1.2.1 Depth calculation without error-correction

This section shows the results of depth deviations which can be observed without applying error corrections. Simulations were established using the ToF simulator. Furthermore raw phase images were captured within the above mentioned preconditions and the distance was calculated according to Equations 2.2 and 2.3 respectively.

Utilizing the improved ToF simulator incorporating the ADC model and the measured illumination waveform the distance deviations were estimated. The modulation waveform was estimated to be pulse-shaped which is just an approximation compared to the actual signal present in the sensor core. Physical parameters of the involved pixel were set to match the module used for actual measurements. The offset error was set to zero and all the other ADC parameters were set to the typical specifications shown in table 3.2. However, 2- and 4-phase evaluation do not yield significant differences due to insufficient modeling of higher order deviations. Simulations were conducted by also incorporating the various noise-sources. Therefore a higher impact of noise in the 2-phase evaluation is visible. Figure 5.1 shows the averaged simulated relative distance deviation of both algorithms with respect to the ground truth. Both figures clearly show the impact of wiggling deviations along the distance sweep which is the result of the non-sinusoidal modulation and illumination signal. It can be seen that the maximum depth deviation with respect to the ground truth is approximately 2 % decreasing with increasing distance.

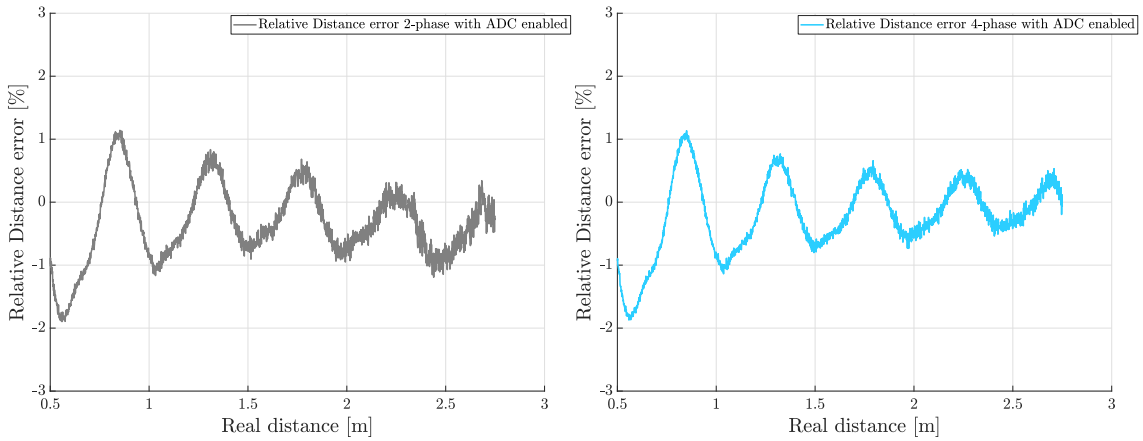

(a) Relative distance deviation of the 2-phase algorithm.

(b) Relative distance deviation of the 4-phase algorithm.

Figure 5.1: Simulated relative distance deviations using an exposure-time of 1ms.

Actual measurement results yield higher deviations when compared to simulation. As mentioned above the model does for example not sufficiently integrate the optical path and the actual modulation waveform. Furthermore varying emission power during exposure of several raw images may cause additional deviations. However, the error curves yield the same shape and frequency. The noise impact in the measurement is even higher at larger distances. This is due to a limiting number of averaging applied to the raw phase images.

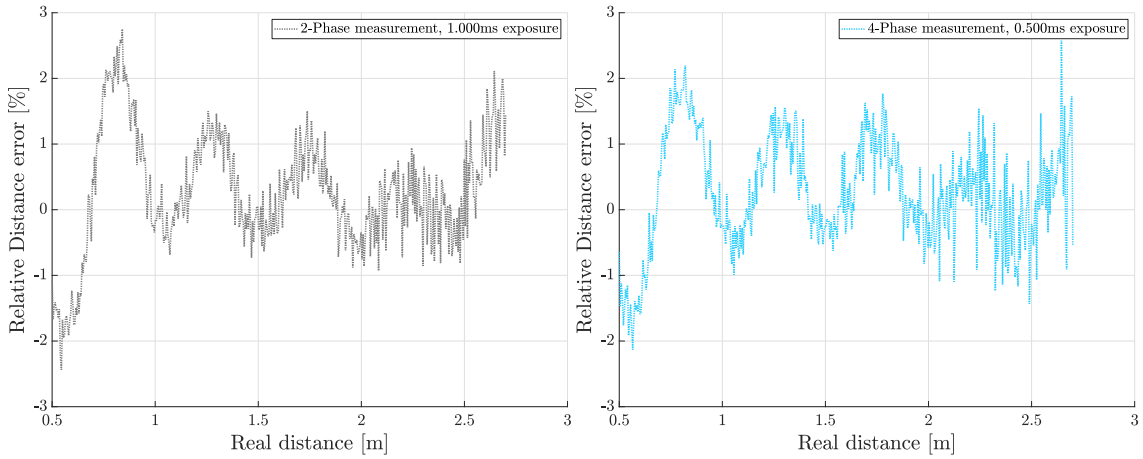

(a) Relative distance deviation of the 2-phase algorithm.

(b) Relative distance deviation of the 4-phase algorithm.

Figure 5.2: Measured relative distance deviations using an exposure-time of 0.5ms and 1ms.

Even when comparing the measured distance sweep results evaluated using the 2- and 4-phase algorithm they do yield high similarities regarding the error curve. In the above defined scenario their error behavior can be considered as the same. As a consequence wiggling calibration was implemented for both algorithms.

5.1.2.2 Depth calculation with enabled error-corrections

By utilizing the wiggling error correction outlined in section 3.3.7.2 both deviation characteristics were stored in a LUT. The behavior can be seen in Figure 3.17a and 3.17b respectively. After depth calculation the correction values were gathered from this table and applied to the calculated phase value. These correction values are independent of the utilized exposure-time and can be used for every distinct integration time setting.

Figure 5.3 shows the result of the wiggling calibrated distance calculation for the 2- and 4-phase algorithms. The relative error is well below 1% in either case. Therefore both yield improved accuracy compared to the uncalibrated measurements shown in Figure 5.2. High-accuracy depth sensing in low background light is therefore possible with both approaches.

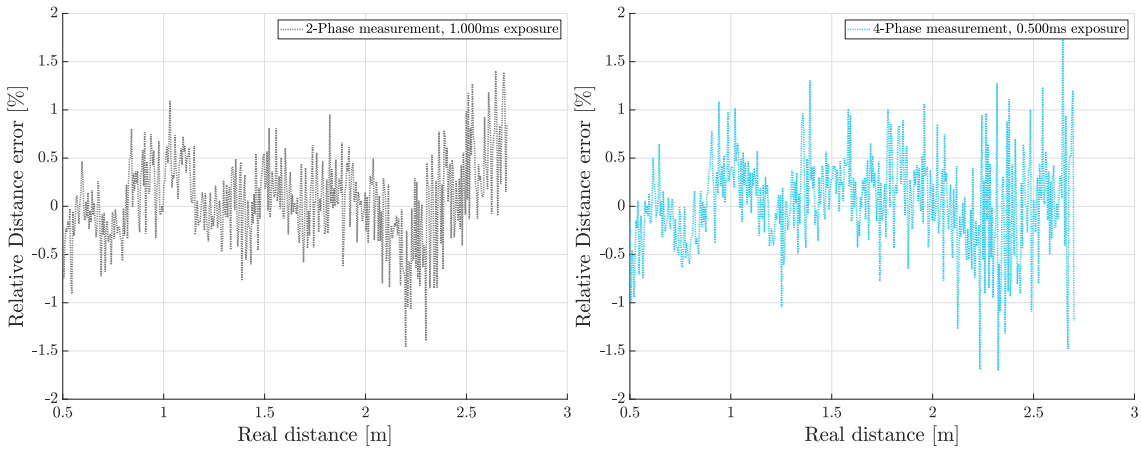

(a) Relative distance deviation of the 2-phase algorithm with applied wiggling correction.

(b) Relative distance deviation of the 4-phase algorithm with applied wiggling correction.

Figure 5.3: Measured relative distance deviations using an exposure-time of 0.5 ms and 1 ms with applied wiggling correction.

In order to quantify the resulting depth error it is advantageous to additionally investigate the absolute error of the measurement. Figure 5.4 shows the error curve in meters during the distance sweep. It is visible that the deviation is beyond one centimeter with some exceptions exceeding this value slightly. A higher influence of noise is visible at a distance of two meters and further. When inspecting Figure 2.11 it can be seen that within low reflected light intensity the read-out noise is becoming the dominant factor. By using the above stated exposure-times it is not possible to reach a light intensity which would diminish the impact of this noise component sufficiently at this distance. Utilizing longer exposure times solves this issue.

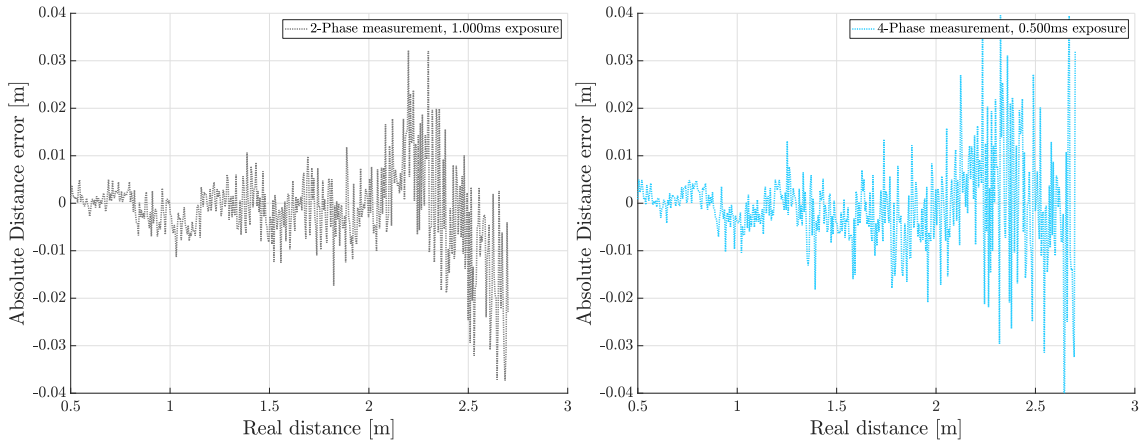

(a) Absolute distance deviation of the 2-phase algorithm with applied wiggling correction.

(b) Absolute distance deviation of the 4-phase algorithm with applied wiggling correction.

Figure 5.4: Measured absolute distance deviations using an exposure-time of 0.5 ms and 1 ms with applied wiggling correction.

The small distance deviations visible in both Figure 5.4a and 5.4b do have very similar nature. Figure 5.5 shows the absolute difference in distance between the 2- and 4-phase evaluation. The resulting error curve yields mainly the noise components which increase because of the subtraction. However, the remaining systematic errors after the correction are mainly canceled out and both algorithms can be considered as yielding the same result for the described measurement scenario. The deviation itself is well beyond 1 cm except of some peaks which are caused by noise.

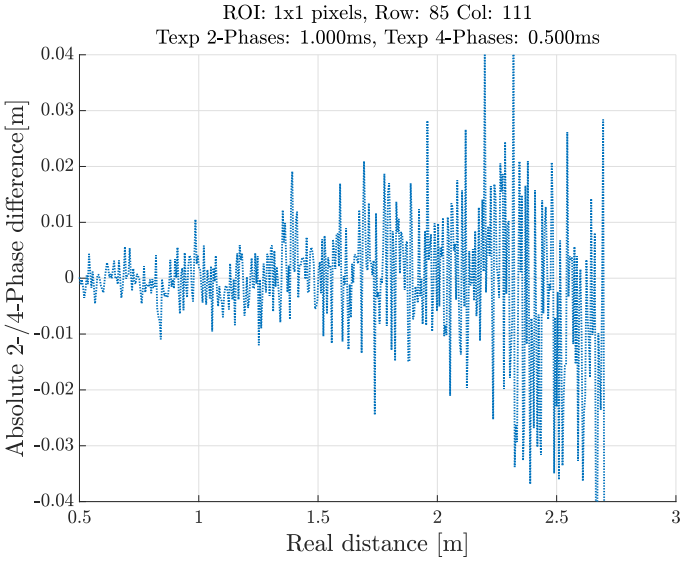

Figure 5.5: Absolute difference between 2- and 4-phase depth measurements.

5.1.2.3 Depth calculation with present background light

The investigation of depth errors in the previous sections was done by excluding the presence of background light. In outdoor scenarios containing direct sunlight would cause the PMD to collect non-correlated photons which can lead to device saturation and limited dynamic range. Consequently the depth calculation yields wrong results. As described in section 2.2.2.1 there is a SBI circuit present in every pixel which effectively reduces the impact of background light. However, the realization of the simplified circuit shown in Figure 2.7 involves transistors which are affected by mismatch. Due to decreasing pixel and subsequently transistor size the impact of this error source increases. As a consequence the SBI circuit introduces integration slope deviations when it is effectively injecting current. Figure 5.6 shows both integration voltages and the error impact on the device operation during the exposure time for 0° and 180° phases.

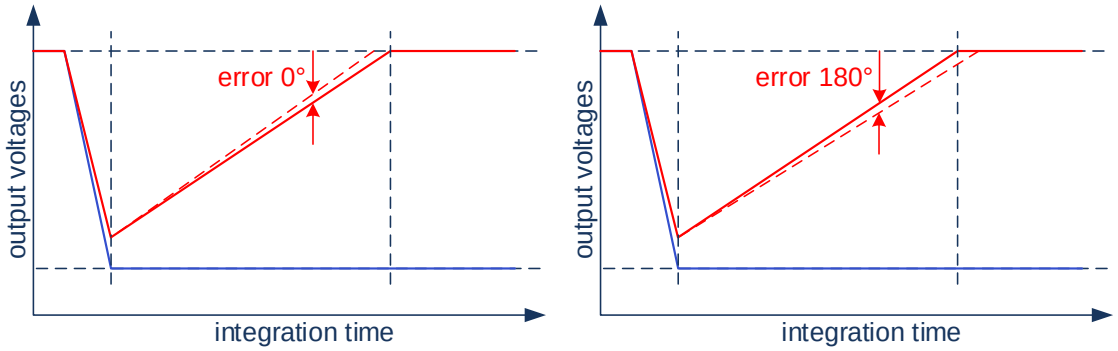

(a) Effect of SBI asymmetry at 0° phase.

(b) Effect of SBI asymmetry at 180° phase.

Figure 5.6: Effect of SBI asymmetry during exposure time.

In section 2.2.2 the differential nature of the pixel is outlined. The usable information therefore is represented by the voltage between the read-out terminals. If one of them reaches the saturation limit, the SBI circuit gets active and preserves the initial voltage. Due to the mentioned mismatch this is not achieved without deviations. As a consequence an altered read-out voltage is sensed by the involved ADC's and subsequent depth errors are introduced. This systematic deviation is canceled out by using the 4-phase algorithm as it can be observed by inspecting Figure 5.6a and 5.6b respectively.

However, by utilizing a 2-phase depth measurement this error has an impact on the depth calculation. The 0°/180° symmetry cannot be exploited. In order to analyze the deviation introduced by the SBI a halogen spotlight was mounted in front of the sensor while conducting a distance sweep. The spectrum of the light emitted by it yields a large amount of infrared and is able to activate the correction circuit. Due to the off-the-shelf nature of the used light-source it was not possible to control the intensity in order to match sunlight behavior. This time the range of the measurement was limited due to the highest intensity residing in the near of the light source. Figure 5.7 shows the calculated depth with respect to the ground truth for the 2- and 4-phase algorithm. The highest deviation is not at the lowest distance due to the light-source not being aligned horizontally with

the sensor. This was done in order to still measure the distance with respect to the white wall. It is visible that the result of the 2-phase measurement is clearly influenced by the SBI assymetry whereas the 4-phase measurement shows no influence of it.

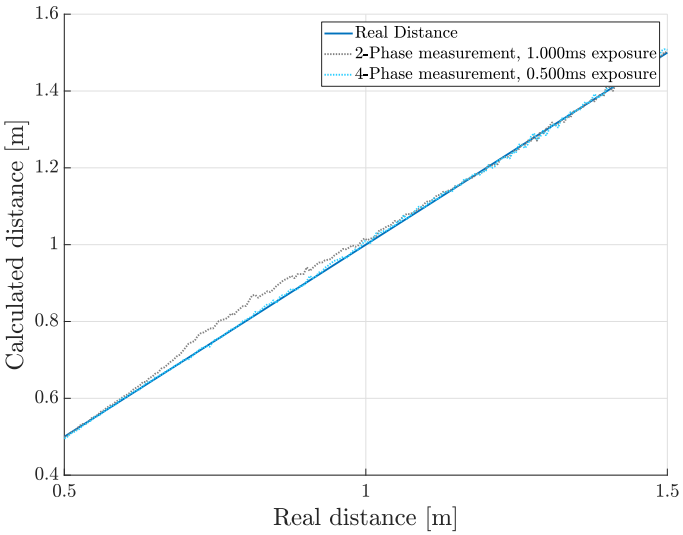

Figure 5.7: Calculated distance of both algorithms with respect to the ground truth in the presence of background light.

Figure 5.8 shows the detailed absolute distance deviations with respect to the ground truth. With the impact of direct light emitted from the off-the-shelf halogen spot, a distance error of up to 4cm is visible. Further measurements with a controllable light source and a known defined spectrum are necessary to exactly quantify depth deviations with respect to light intensity. Thus the impact of sunlight in outdoor scenarios can be exactly determined and quantified.

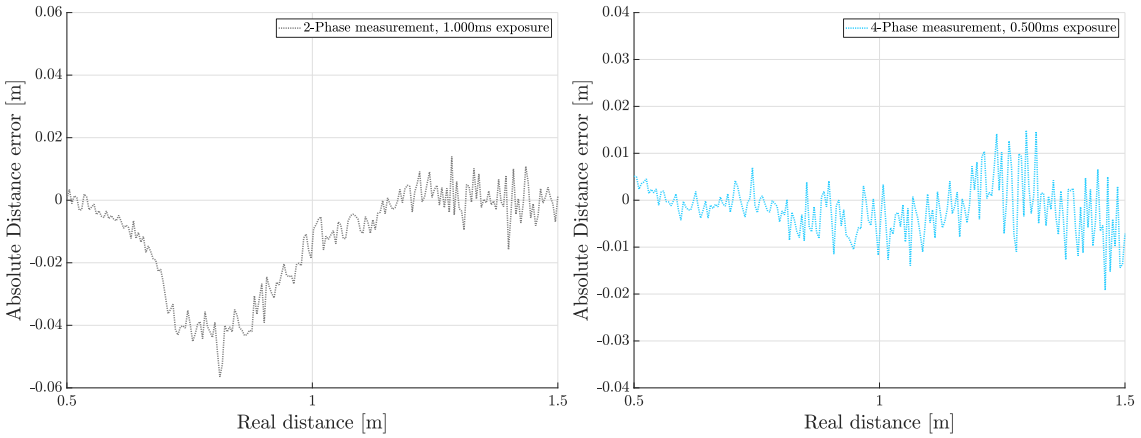

(a) Absolute distance deviation of the 2-phase algorithm.

(b) Absolute distance deviation of the 4-phase algorithm.

Figure 5.8: Measured absolute distance deviations using an exposure-time of 0.5 ms and 1 ms with applied wiggling correction in the presence of background light.

The limitations of the 2-phase algorithm are revealed in the presence of background light. Sections 5.1.2.1 and 5.1.2.2 may imply that both algorithms yield almost the same result with respect to the overall accuracy. However, in this section the clear impact of background light and its effect on the pixel voltage and subsequent depth calculation was shown. This introduced systematic error cannot be compensated without repeatedly measuring the background light intensity. Thus outdoor scenarios may yield significant deviations between the two algorithms. Furthermore the SBI circuit is also activated if pixels are about to saturate due to the emission of the build-in VCSEL. As a consequence the effect may show itself even if there is no present background light.

5.1.3 Spatial evaluation of depth data

By evaluating the depth of all pixels inside the image sensor a 3D Scene can be captured. Both 2- and 4-phase algorithms were utilized for establishing the depth images in Figure 5.9. It shows a head measured with a distance of approximately 20 cm.

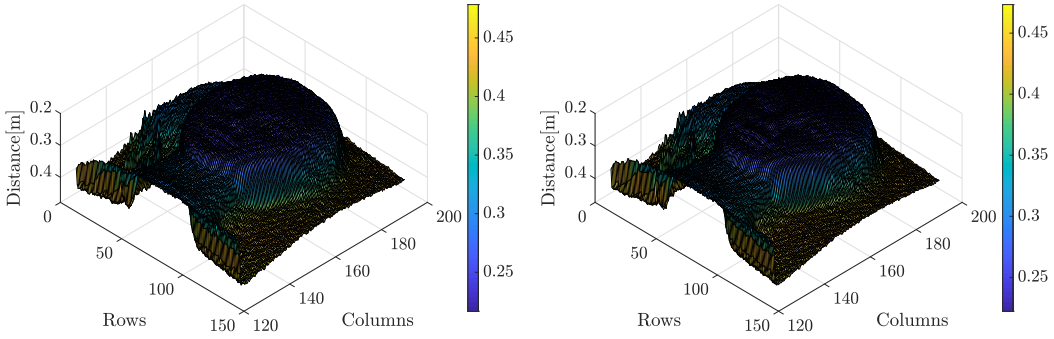

(a) Absolute distance deviation of the 2-phase algorithm.

(b) Absolute distance deviation of the 4-phase algorithm.

Figure 5.9: Measured absolute distance deviations using an exposure-time of 0.5 ms and 1 ms with applied wiggling correction in the presence of background light.

It can be seen that after applying the respective corrections, 2- and 4-phase algorithm both yield results within the same range. Face details are clearly visible and subsequent face recognition algorithms can be applied. Figure 5.10 shows the error surface when comparing both algorithms. When evaluating the error values within a centered square of 20x20 pixels, the mean is 0.5 cm. This corresponds to the distance sweep results in Figure 5.5.

However, higher deviations are observable outside the area covered by the face. This is mainly due to stray-light which is the result when measuring fine-grained hair which causes diffuse reflections. Moreover no lens-corrections were applied due to imperfect mounting of the lens. Furthermore it is necessary to apply FPPN compensation after lens-corrections. When inspecting the rows axis in Figure 5.10 it can be seen that it is not in parallel with the surface like it is in the columns axis. This is an effect caused by mounting of the lens mentioned before. These error sources affect both evaluation

algorithms in the same way and have to be compensated. As a consequence utilizing the proposed processing architecture it is possible to reduce the overall power consumption while still providing high-accuracy depth images for face recognition. However, this is limited to an environment with low background light.

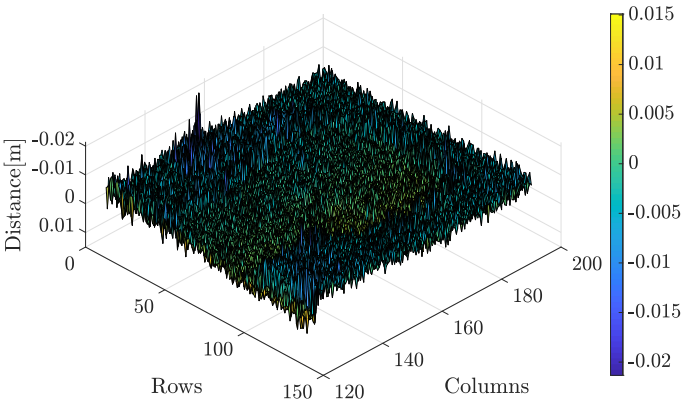

Figure 5.10: Difference between 2- and 4-phase surface measurement.

5.2 Power profile of the proposed architecture

The power profile of the proposed architecture can be gathered by monitoring the current which is consumed by the sensor itself. However, a ToF system consists of several components which closely interact with each other. As depicted in Figure 3.21 it inherits a cx-3 communication chip which is responsible for transferring data between the image sensor and the host PC. By simply measuring the overall current consumption it is not possible to gather the amount of energy consumed by the sensor alone due to the cx-3 chip being active as well. Therefore it is required to directly access the supply rails of the image sensor.

Due to the need of a drastic hardware change the above mentioned method was not applied. The respective power consumption values of the different sensor use-cases were already mentioned in table 3.1. Based on these values, the power profile can be estimated. The proposed low-power architecture is utilizing a Mode 2 use-case operating at 1 FPS. However, as the main contribution of power-consumption is due to the idle state, the sensor is completely shut-down after the readout as it is stated in Figure 3.23. As a result the overall power-consumption reduces to 1mW depending on the specified exposure time. This marks a theoretical value as the repeated start-up is not considered. Furthermore periodically loading of the sensor configuration from flash memory additionally alters this value. By inspecting table 2.1, it is visible that the power consumption of the proposed low-power architecture delivers similar results when compared to existing proximity sensing solutions. Nevertheless the specifications yield a higher measurement frequency and their respective power profile can be reduced by adjusting it.

Chapter 6

Conclusion

Due to the decreasing size of ToF image sensors, they are now utilized in mobile devices and are able to provide highly accurate depth maps of the surrounding scene. Several applications including auto-focus or face unlock use this technology in order to improve the user experience. However, low-power proximity measurement modes are needed when operating in such environments. The aim of this thesis is to find a suitable architecture which is capable of providing depth information while lowering the overall power consumption of the imaging device. By reducing the number of raw frames by half, a substantial reduction can be achieved. However, this leads to systematic errors influencing the depth calculation. An existing model of the ToF sensor was extended and adjusted to simulate the impact of these errors on the subsequent depth calculation. Therefore an ADC model incorporating the DC deviations was designed and the measured illumination waveform was integrated in the simulation environment.

Based on the foregoing investigations, correction mechanisms were introduced to compensate for the impact of the deviations effectively altering the depth measurement. To achieve that, a calibration method was designed to acquire the errors caused by the non-sinusoidal modulation and illumination signal. Furthermore offset compensation values were extracted to eliminate the FPN which shows high impact on subsequent post-processing. After error-correction of the proposed 2-phase operation it shows similar performance compared to the well-known 4-phase processing. Therefore this algorithm was chosen for the low-power architecture. By effectively eliminating the idle time in the measurement, the overall power consumption can be reduced drastically. This is achieved by repeatedly powering-down the sensor in between frames. Furthermore a 2-phase operation decreases the number of sensor readout's by half. The proposed solution was implemented by means of a Python program including a GUI. Error-corrections, depth algorithms and exposure times can be selected by the user and the resulting depth image is presented by means of a color-mapped visualization.

By utilizing the proposed solution, low-power operation is ensured while still providing depth images. The resulting power profile is similar to existing proximity sensors and is theoretically able to take over their functionality. However, the power consumption during the start-up of the imaging device has to be additionally investigated. Furthermore the established approach is limited regarding the presence of background light. When operating the imaging system within bright conditions(e.g. sunlight), depth deviations are introduced due to the asymmetry of the SBI circuit inside the PMD.

6.1 Future Work

Within this thesis, a low-power indirect ToF sensing approach was developed. It focused on an existing image sensor within a fixed system environment. However, the power consumption also depends on the involved sensor hardware. In the following some suggestions for improvements are outlined.

- In a proximity sensing environment it is not necessary to gather the data of the whole pixel array. Partial read-out of the sensor core decreases the amount of active ADC's involved. Furthermore it reduces the pixel data which has to be transmitted. This measurement mode can be established by a firmware change.
- The idle power consumption plays an important role when operating at low FPS. Therefore optimization on circuit level could improve the situation and eliminate the need of constantly switching off the sensor core.
- Hardware binning also reduces the amount of data which has to be transferred and improves the performance at low-exposure times. It is a technique which combines the accumulated charges of several pixels. As a consequence the resolution is decreased, but the overall SNR is improved.
- Optimization of the signal path and pixel architecture could improve the impact of FPN. This would result in less effort involved in post-processing of a 2-phase measurement.

Acronyms

AC Alternating Current. 23, 34

ADC Analog Digital Converter. 6, 12, 17, 20, 23, 30–32, 34–40, 43–45, 50, 56, 57, 62, 64, 66, 70, 75, 76

ams Austria Microsystems. 24, 25

API Application Programming Interface. 59

CCD Charge-coupled device. 11

CMOS Complementary Metal-oxide semiconductor. 11, 24, 25

CSI Camera Serial Interface. 6

CW Continuous-Wave. 1, 5, 11, 15

DC Direct-current. 11, 13, 17, 34, 35, 39, 47, 57, 75

DNL Differential non-linearity. 32, 35, 39, 40

ENOB Effective number of bits. 23

FoV Field of view. 48

FPN Fixed Pattern Noise. 17, 18, 27, 34, 37, 42–46, 50, 59, 61, 64, 65, 75, 76

FPPN Fixed Pattern Phase Noise. 18, 63, 72

FPS Frames Per Second. 29, 30, 53, 73, 76

FSR Full-scale range. 31, 35, 39

GPIO General-purpose input/output. 53

GPS Global Positioning System. 21

GUI Graphical User Interface. 52–54, 56, 64, 75

HF High-Frequency. 18

I2C Inter-integrated circuit. 51, 53, 64

IDE Intregrated development environment. 56

INL Integral non-linearity. 31, 34, 35, 38, 39

IoT Internet of Things. 22

IR Infrared. 2, 10, 23

LED Light-emitting diode. 23

LSB Least significant bit. 17, 31, 35, 37, 39, 40, 43, 57, 64

LTS Linear Translation Stage. 40, 48, 49, 56, 59, 62

LUT Lookup table. 17, 27, 46, 47, 50, 68

MIPI Mobile Industry Processor Interface Alliance. 6, 30, 51, 55

MOS Metal-oxide semiconductor. 11

PC Personal Computer. 21, 48, 51, 55, 73

PCB Printed Circuit Board. 55

PMD Photonic Mixing Device. 3, 5, 9–15, 17, 19, 20, 25, 30, 46, 56, 70, 75

PRNU Photo-response non-uniformity. 17

SAR Successive Approximation Register. 20

SBI Suppression of Background Illumination. 13, 70–72, 75

SDK Software Development Kit. 56

SNR Signal-to-Noise Ratio. 10, 21, 65, 66, 76

SoC System-on-Chip. 21

SPAD Single-photon avalanche diode. 24–26

SPI Serial Peripheral Interface. 51, 53, 54, 56, 64

TDC Time-to-digital converter. 24, 26

TIA Transimpedance Amplifier. 23

ToF Time-of-Flight. 1–3, 5, 6, 8, 14–17, 21, 24, 25, 27–30, 34, 37, 48, 55–57, 59, 66, 73, 75, 76

UAV Unmanned Aerial Vehicle. 25

USB Universal Serial Bus. 48, 51, 55

VCSEL Vertical-cavity surface-emitting Laser. 5, 12, 29, 47, 51, 55, 56, 58, 72

Chapter 7

Bibliography

[Alb07] Martin Albrecht. Untersuchung von Photogate-PMD-Sensoren hinsichtlich qualifizierender Charakterisierungsparameter und-methoden. 2007.

[All18] Matthias Allmer. Time-of-Flight 3D Camera Performance Modeling. Master's thesis, Graz University of Technology, 2018.

[BBMP10] Sebastiano Battiato, Arcangelo Ranieri Bruna, Giuseppe Messina, and Giovanni Puglisi. *Image processing for embedded devices.* Bentham Science Publishers, 2010.

[BP17] S. Bosse and E. Pournaras. An Ubiquitous Multi-agent Mobile Platform for Distributed Crowd Sensing and Social Mining. In *2017 IEEE 5th International Conference on Future Internet of Things and Cloud (FiCloud)*, pages 280–287, Aug 2017.

[BR16] A. Bhandari and R. Raskar. Signal Processing for Time-of-Flight Imaging Sensors: An introduction to inverse problems in computational 3-D imaging. *IEEE Signal Processing Magazine*, 33(5):45–58, Sep. 2016.

[Cen] Pew Research Center. Cellphones, Computers Are the Most Commonly Owned Devices. `https://www.pewinternet.org/2015/10/29/technology-device-ownership-2015/pi_2015-10-29_device-ownership_0-03/`. Accessed: 2019-06-24.

[CGL+96] S. Cova, M. Ghioni, A. Lacaita, C. Samori, and F. Zappa. Avalanche photodiodes and quenching circuits for single-photon detection. *Appl. Opt.*, 35(12):1956–1976, Apr 1996.

[CMT+08] Sunny Consolvo, David W McDonald, Tammy Toscos, Mike Y Chen, Jon Froehlich, Beverly Harrison, Predrag Klasnja, Anthony LaMarca, Louis LeGrand, Ryan Libby, et al. Activity sensing in the wild: a field trial of ubifit garden. In *Proceedings of the SIGCHI conference on human factors in computing systems*, pages 1797–1806. ACM, 2008.

[dCC+18] T. C. de Albuquerque, F. Calmon, R. Clerc, P. Pittet, Y. Benhammou, D. Golanski, S. Jouan, D. Rideau, and A. Cathelin. Integration of SPAD in 28nm FDSOI CMOS technology. In *2018 48th European Solid-State Device Research Conference (ESSDERC)*, pages 82–85, Sep. 2018.

[Depa] Statista Research Department. Number of mobile phone users worldwide from 2015 to 2020. https://www.statista.com/statistics/274774/forecast-of-mobile-phone-users-worldwide/. Accessed: 2019-06-24.

[Depb] Statista Research Department. Percentage of all global web pages served to mobile phones from 2009 to 2018. https://www.statista.com/statistics/241462/global-mobile-phone-website-traffic-share/. Accessed: 2019-06-24.

[Ein65] Albert Einstein. Concerning an heuristic point of view toward the emission and transformation of light. *American Journal of Physics*, 33(5):367, 1965.

[Gru13] Johannes Gruenwald. Investigation of Systematic Errors in Time-of-Flight Imaging. Master's thesis, Graz University of Technology, 2013.

[HLCH12] Miles Hansard, Seungkyu Lee, Ouk Choi, and Radu Patrice Horaud. *Time-of-flight cameras: principles, methods and applications*. Springer Science & Business Media, 2012.

[Jah09] Jürgen Jahns. *Photonik: Grundlagen, Komponenten und Systeme*. Walter de Gruyter, 2009.

[JCPD10] A. P. P. Jongenelen, D. A. Carnegie, A. D. Payne, and A. A. Dorrington. Maximizing precision over extended unambiguous range for TOF range imaging systems. In *2010 IEEE Instrumentation Measurement Technology Conference Proceedings*, pages 1575–1580, May 2010.

[JHG99a] Bernd Jähne, Horst Haussecker, and Peter Geissler. *Handbook of computer vision and applications*, volume 3. Citeseer, 1999.

[JHG99b] Bernd Jähne, Horst Haussecker, and Peter Geissler. *Handbook of computer vision and applications*, volume 1. Citeseer, 1999.

[JM08] David A Johns and Ken Martin. *Analog integrated circuit design*. John Wiley & Sons, 2008.

[KKC19] J. Kwak, J. Kim, and S. Chong. Proximity-Aware Location Based Collaborative Sensing for Energy-Efficient Mobile Devices. *IEEE Transactions on Mobile Computing*, 18(2):417–430, Feb 2019.

[Lab] AQUA Laboratory. Simplified block diagram of a direct Time-of-Flight sensor system. https://aqua.epfl.ch/research/single-photon-sensor-architectures/page-157535-en-html/. Accessed: 2019-09-17.

[Lan06] Robert Lange. 3D time-of-flight distance measurement with custom solid-state image sensors in CMOS/CCD-technology. 2006.

[LBB+19] N. Laković, M. Brkić, B. Batinić, J. Bajić, V. Rajs, and N. Kulundžić. Application of low-cost VL53L0X ToF sensor for robot environment detection. In *2019 18th International Symposium INFOTEH-JAHORINA (INFOTEH)*, pages 1–4, March 2019.

[LKR08] M. Lindner, A. Kolb, and T. Ringbeck. New insights into the calibration of ToF-sensors. In *2008 IEEE Computer Society Conference on Computer Vision and Pattern Recognition Workshops*, pages 1–5, June 2008.

[LML+10] N. D. Lane, E. Miluzzo, H. Lu, D. Peebles, T. Choudhury, and A. T. Campbell. A survey of mobile phone sensing. *IEEE Communications Magazine*, 48(9):140–150, Sep. 2010.

[LSKK10] Marvin Lindner, Ingo Schiller, Andreas Kolb, and Reinhard Koch. Time-of-Flight sensor calibration for accurate range sensing. *Computer Vision and Image Understanding*, 114(12):1318–1328, 2010.

[Lua01] Xuming Luan. Experimental investigation of photonic mixer device and development of TOF 3D ranging Systems based on PMD technology, 2001.

[MRS+09] Min Mun, Sasank Reddy, Katie Shilton, Nathan Yau, Jeff Burke, Deborah Estrin, Mark Hansen, Eric Howard, Ruth West, and Péter Boda. PEIR, the Personal Environmental Impact Report, As a Platform for Participatory Sensing Systems Research. In *Proceedings of the 7th International Conference on Mobile Systems, Applications, and Services*, MobiSys '09, pages 55–68, New York, NY, USA, 2009. ACM.

[OSY+13] C. Otani, Y. Sasaki, T. Yuasa, M. Suga, H. Kasuga, and H. Ohmori. THz 3D imaging with phase-shifting interferometry. In *2013 Conference on Lasers and Electro-Optics Pacific Rim (CLEOPR)*, pages 1–2, June 2013.

[PJD+09] Andrew D Payne, Adrian PP Jongenelen, Adrian A Dorrington, Michael J Cree, and Dale A Carnegie. Multiple frequency range imaging to remove measurement ambiguity. In *Optical 3-d measurement techniques*, 2009.

[Pla06] Matthias Plaue. Technical report: Analysis of the PMD imaging system. *Interdisciplinary Center for Scientific Computing, University of Heidelberg*, 2006.

[Sch05] Bernd Schneider. Der Photomischdetektor zur schnellen 3D-Vermessung für Sicherheitssysteme und zur Informationsübertragung im Automobil. 2005.

[SFS+16] L. Sant, A. Fant, S. Stojanović, S. Fabbro, and J. L. Ceballos. A 13.2 b Optical Proximity Sensor System With 130 klx Ambient Light Rejection Capable of Heart Rate and Blood Oximetry Monitoring. *IEEE Journal of Solid-State Circuits*, 51(7):1674–1683, July 2016.

[SN06] Simon M Sze and Kwok K Ng. *Physics of semiconductor devices*. John wiley & sons, 2006.

[SP18] W. Shi and A. Pan. Mixed Design of SPAD Array Based TOF for Depth Camera and Unmanned Vehicle Applications. In *2018 15th International Conference on Synthesis, Modeling, Analysis and Simulation Methods and Applications to Circuit Design (SMACD)*, pages 277–280, July 2018.

[STHD17] J. Steinbaeck, A. Tengg, G. Holweg, and N. Druml. A 3D Time-of-Flight Mixed-Criticality System for Environment Perception. In *2017 Euromicro Conference on Digital System Design (DSD)*, pages 368–374, Aug 2017.

[TVS+17] A. K. Triantafyllidis, C. Velardo, D. Salvi, S. A. Shah, V. G. Koutkias, and L. Tarassenko. A Survey of Mobile Phone Sensing, Self-Reporting, and Social Sharing for Pervasive Healthcare. *IEEE Journal of Biomedical and Health Informatics*, 21(1):218–227, Jan 2017.

[VCR17] I. Vornicu, R. Carmona-Galán, and A. Rodríguez-Vázquez. Photon counting and direct ToF camera prototype based on CMOS SPADs. In *2017 IEEE International Symposium on Circuits and Systems (ISCAS)*, pages 1–4, May 2017.

[vVGK06] W. van der Tempel, D. Van Nieuwenhove, R. Grootjans, and M. Kuijk. An Active Demodulation Pixel using a Current Assisted Photonic Demodulator Implemented in 0.6um Standard CMOS. In *3rd IEEE International Conference on Group IV Photonics, 2006.*, pages 116–118, Sep. 2006.

[ZZ10] Horst Zimmermann and H Zimmermann. *Integrated silicon optoelectronics*, volume 148. Springer, 2010.